J. Fluid Mech. (2011), *vol.* 667, *pp.* 272–308.
doi:10.1017/S0022112010004453

Triggering in the horizontal Rijke tube: non-normality, transient growth and bypass transition

MATTHEW P. JUNIPER†

Department of Engineering, University of Cambridge, Trumpington Street, Cambridge CB2 1PZ, UK

(Received 23 November 2009; revised 13 August 2010; accepted 17 August 2010; first published online 25 November 2010)

With a sufficiently large impulse, a thermoacoustic system can reach self-sustained oscillations even when it is linearly stable, a process known as triggering. In this paper, a procedure is developed to find the lowest initial energy that can trigger self-sustained oscillations, as well as the corresponding initial state. This is known as the 'most dangerous' initial state. The procedure is based on adjoint looping of the nonlinear governing equations, combined with an optimization routine. It is developed for a simple model of a thermoacoustic system, the horizontal Rijke tube, and can be extended to more sophisticated thermoacoustic models. It is observed that the most dangerous initial state grows transiently towards an unstable periodic solution before growing to a stable periodic solution. The initial energy required to trigger these self-sustained oscillations is much lower than the energy of the oscillations themselves and slightly lower than the lowest energy on the unstable periodic solution. It is shown that this transient growth arises due to non-normality of the governing equations. This is analogous to the sequence of events observed in bypass transition to turbulence in fluid mechanical systems and has the same underlying cause. The most dangerous initial state is calculated as a function of the heat-release parameter. It is found that self-sustained oscillations can be reached over approximately half the linearly stable domain. Transient growth in real thermoacoustic systems is 10^5–10^6 times greater than that in this simple model. One practical conclusion is that, even in the linearly stable regime, it may take very little initial energy for a real thermoacoustic system to trigger to high-amplitude self-sustained oscillations through the mechanism described in this paper.

Key words: acoustics, instability, transition to turbulence

1. Introduction

It is well known that the laminar flow in a round pipe becomes turbulent at a Reynolds number between 1000 and 10 000. It is also well known that this laminar flow has no unstable eigenvalues at any Reynolds number. How then can small perturbations grow? The likely mechanism is summarized by Trefethen *et al.* (1993), following work by Butler & Farrell (1992) and Reddy & Henningson (1993). It has become known as bypass transition to turbulence because it bypasses traditional stability theory's requirement for an unstable eigenvalue. The mechanism relies on

† Email address for correspondence: mpj1001@cam.ac.uk

the fact that the linear stability operator is non-normal. This means that certain perturbations can grow transiently even when the system is linearly stable. These then trigger turbulence through nonlinear mechanisms. A review of this research and more recent developments in the field can be found in Schmid (2007).

There is an analogous mechanism in thermoacoustics, through which a small perturbation evolves to high-amplitude self-sustained oscillations even when the unperturbed system has no unstable eigenvalues. This is known as triggering. It has been observed in solid rocket motors, liquid rocket motors and laboratory experiments. It is summarized in Zinn & Lieuwen (2005) (p. 19): *'Although large-amplitude disturbances are generally required to initiate unstable oscillations in nonlinearly unstable systems, a system may be nonlinearly unstable at low-amplitude disturbances that are of the order of the background noise level. This scenario is somewhat analogous to the hydrodynamic stability of a laminar Poiseuille flow'*. Although flow instability differs from thermoacoustics and turbulence differs from self-sustained oscillations, the two situations are both non-normal and nonlinear, which suggests that bypass transition and triggering could be similar. The broad aim of this paper is to use the framework of bypass transition in fluid mechanics to provide a stronger link between studies of non-normality and studies of nonlinearity in thermoacoustics, such as Balasubramanian & Sujith (2008*a*) and Ananthkrishnan, Deo & Culick (2005).

1.1. *Bypass transition and the failure of linear analysis in hydrodynamics*

The stability of a laminar flow is often investigated by calculating the eigenvalues of small linear perturbations to that flow. If at least one eigenvalue is unstable, then the flow is linearly unstable. If all eigenvalues are stable, then the flow is linearly stable. The critical parameter between these two states (usually a Reynolds number) can be calculated and it might seem sensible to assume that this is the critical parameter for the onset of turbulence.

Unfortunately, this technique often fails. For instance, Hagen–Poiseuille flow is linearly stable at all Reynolds numbers but becomes turbulent at $Re \approx 2000$. Plane Poiseuille flow is linearly stable up to $Re = 5772$ but becomes turbulent at $Re \approx 1000$. Plane Couette flow is linearly stable at all Reynolds numbers but becomes turbulent at $Re \approx 360$. One notable success is Benard convection, which is linearly stable up to $Re \approx 1708$ and becomes turbulent also around $Re \approx 1700$.

Eigenvalue analysis fails in the first three flows because their linearized stability operators are non-normal. It succeeds in the fourth flow because its linearized stability operator is normal. (A matrix or operator $\boldsymbol{L}$ is normal, or self-adjoint, if it satisfies $\boldsymbol{L}^{+}\boldsymbol{L} = \boldsymbol{L}\boldsymbol{L}^{+}$, where $\boldsymbol{L}^{+}$ is the adjoint of $\boldsymbol{L}$.) Non-normal stability operators can cause very high transient growth, typically 10^4–10^6 times the initial perturbation energy, even in situations that are linearly stable (Schmid & Henningson 2001). This transient growth is a key component of bypass transition in the first three flows.

In flow instability, Schmid & Henningson (2001) divide bypass transition into five stages. The first stage is initiation of small perturbations to the flow. The second stage is linear amplification of these perturbations due to non-normal growth. The third stage is nonlinear saturation towards a new steady or quasi-steady periodic state. The fourth stage is growth of secondary instabilities on top of this periodic base flow. The fifth stage is breakdown to turbulence, where nonlinearities and/or symmetry-breaking instabilities excite an increasing number of scales in the flow. This idealization provides a useful framework with which to view bypass transition, even for complicated flows.

A flow can also be considered as a dynamical system, as in Skufca, Yorke & Eckhardt (2006) for parallel shear flow and Schneider, Eckhardt & Yorke (2007) and Duguet, Willis & Kerswell (2008) for pipe flow. A boundary in state space is identified between trajectories that decay to a laminar solution and trajectories that evolve to a turbulent solution. Trajectories that are attracted to this boundary from lower energy states exhibit the transient growth identified in stage 2. Having identified this boundary, which Skufca *et al.* (2006) call the 'edge of chaos', stage 4 can be described in more detail. This boundary contains several heteroclinic saddle points and at least one local relative attractor, each corresponding to a periodic travelling-wave solution (Duguet, Willis & Kerswell 2008). The state wanders from the vicinity of one travelling-wave solution to the vicinity of another and so on until it reaches a local relative attractor, where it either evolves towards the laminar solution or towards a turbulent solution. Its final state very sensitively depends on its initial state. The travelling-wave solutions correspond to the quasi-steady periodic state identified in stage 3 of Schmid & Henningson (2001).

1.2. *Triggering and the need for nonlinearity and non-normality in thermoacoustics*

In this paper, a similar conceptual framework is applied to thermoacoustic triggering, which also involves non-normality and nonlinearity. The role of nonlinearity is summarized by Ananthkrishnan *et al.* (2005), who show that the system must have either a subcritical bifurcation or a supercritical bifurcation followed by a fold bifurcation in order to trigger. This is similar to the requirements for bypass transition (Henningson & Reddy 1994). In such a system, there are two (or more) stable solutions to the governing equations. The first is a stable fixed point at zero amplitude and the second is a stable periodic solution at finite amplitude. When the system is at the stable fixed point, a sufficiently large impulse can knock it into the basin of attraction of the self-sustained oscillation. This is triggering. Such systems are sometimes called 'linearly stable but nonlinearly unstable' (Zinn & Lieuwen 2005), but it should be stressed that, from a dynamical systems' point of view, both solutions are stable.

Noiray *et al.* (2008) present a practical and novel method to predict whether a system will be susceptible to triggering. They measure the flame's OH^* emission as a function of forcing frequency and amplitude, from which they interpolate to obtain a flame describing function (FDF). Then they enter this into a frequency-domain nonlinear stability analysis to predict the self-excited behaviour of the system. They validate this against the experimentally observed self-excited behaviour and thereby account for the nonlinear aspects of triggering, mode switching and hysteresis. In a system that is susceptible to triggering, an unstable periodic solution sits on the boundary between the basins of attraction of the stable fixed point and the stable periodic solution (§ 3.2). This is the steady or quasi-steady periodic state described in stage 3 of § 1.1. The results in figure 9 of Noiray *et al.* (2008) show that the system triggers when its amplitude infinitesimally exceeds that of this unstable periodic solution, corresponding to stage 4 of § 1.1. Their study, however, freezes harmonics to the fundamental mode. It will be shown in § 3.4 that this precludes non-normal transient growth, which means that their method cannot account for the growth towards the periodic state described in stage 2 of § 1.1. To account for this growth, non-normality must also be considered.

The role of non-normality in thermoacoustics was first considered by Balasubramanian & Sujith (2008*a*) for the Rijke tube, by Balasubramanian & Sujith (2008*b*) for a Burke–Schumann flame in a tube and by Nagaraja, Kedia & Sujith (2009) for a generic n–τ combustion model. These papers show that the

linearized governing equations are non-normal, which means that their corresponding eigenvectors are non-orthogonal. This is a general feature of eigenvectors in thermoacoustics (Nicoud *et al.* 2007), and means that some initial states are composed of eigenfunctions with large amplitudes that largely cancel out. If the eigenfunctions of such states decay at different rates, the states grow initially even if all the eigenfunctions eventually decay (Schmid 2007). Using linear algebra, Balasubramanian & Sujith (2008*a*) found the states that have maximum transient growth away from the stable fixed point and, using nonlinear time marching, showed that these states can grow to self-sustained oscillations in a linearly stable system. This paper examines this process in more detail and, in particular, examines the states that cause maximum transient growth towards the unstable periodic solution.

1.3. *The structure of this paper*

This paper examines the simple model of thermoacoustic oscillations in the horizontal Rijke tube studied by Balasubramanian & Sujith (2008*a*). Although this model is much less complex than real thermoacoustic systems, it contains important elements of real systems, such as a time delay between velocity and heat-release perturbations as well as a heat-release rate that depends nonlinearly on the velocity. Usually, the nonlinear governing equations are used but, occasionally, the linear equations are required. The model and the linearizations are described in § 2.1, together with the three thermoacoustic systems that are used as examples.

A classical nonlinear analysis is performed in § 3. The systems' bifurcation diagrams are plotted as a function of the heat-release parameter. A continuation method is used to find the periodic solutions, whose stability is determined from their Floquet multipliers. Careful consideration of the basins of attraction of the periodic solutions reveals the role that the unstable periodic solution plays in the triggering process.

Previous studies have considered linear transient growth around the stable fixed point. In § 3.3, linear transient growth is considered around the unstable periodic solution, which is more relevant to triggering. A linear analysis is limited to the vicinity of the unstable periodic solution; so, in § 4, a procedure is developed to find optimal initial states of the nonlinear governing equations. This is used to find the initial states that trigger to self-sustained oscillations from the lowest possible energy, which are called the 'most dangerous' initial states.

Having found these states, the linear evolution and nonlinear evolution are compared in § 5 in order to determine whether the transient growth is caused by non-normality, nonlinearity, or some combination of the two. The triggering process is then compared with that of bypass transition within the framework introduced in § 1.1 and found to be similar but simpler.

In § 6, the procedure is applied over the full range of the heat-release parameter at which the system is susceptible to triggering. This gives the bound, in terms of the initial perturbation energy, below which the system can never trigger to self-sustained oscillations, which is called the 'safe operating region'. In more complex systems, this bound will have important engineering significance.

It turns out that the thermoacoustic system in this paper has two stable periodic solutions. In §§ 3–6, the concepts are described with reference to the first solution. In § 7, the second solution is introduced.

This paper describes an idealized situation, in which triggering occurs from a well-defined initial state in a noiseless system. It could be difficult to create such a system in the laboratory; so the implications for experiments, in particular the effect of different types of noise, are discussed in § 8.

2. The model and its governing equations

2.1. *The dimensional governing equations*

The thermoacoustic system examined in this paper, a horizontal Rijke tube, is identical to that studied by Balasubramanian & Sujith (2008*a*). This is a tube of length L_0 in which a hot wire is placed distance $\tilde{x}_f$ from one end. A base flow is imposed through the tube with velocity u_0. The physical properties of the gas in the tube are described by c_v, γ, R and λ, which represent the constant volume specific heat capacity, the ratio of specific heats, the gas constant and the thermal conductivity, respectively. The unperturbed quantities of the base flow are ρ_0, p_0 and T_0, which represent density, pressure and temperature, respectively. From these, one can derive the speed of sound $c_0 \equiv \sqrt{\gamma R T_0}$ and the Mach number of the flow $M \equiv u_0/c_0$.

Acoustic perturbations are considered on top of this base flow. In dimensional form, the perturbation velocity and perturbation pressure are represented by the variables $\tilde{u}$ and $\tilde{p}$, respectively, and distance and time are represented by the coordinates $\tilde{x}$ and $\tilde{t}$, respectively. Quantities evaluated at the hot wire's position, $\tilde{x}_f$, have subscript f. At the hot wire, the rate of heat transfer to the gas is given by $\tilde{Q}$. This heat transfer is applied at the wire's position by multiplying $\tilde{Q}$ by the dimensional Dirac delta distribution $\tilde{\delta}_D(\tilde{x}-\tilde{x}_f)$. (The subscript D distinguishes the Dirac delta from a small variation δ in Appendix A.) Acoustic damping, which will be described in § 2.4, is represented by ζ.

The dimensional governing equations for the perturbation comprise the momentum equation and the energy equation:

$$\tilde{F}_1 \equiv \rho_0 \frac{\partial \tilde{u}}{\partial \tilde{t}} + \frac{\partial \tilde{p}}{\partial \tilde{x}} = 0, \tag{2.1}$$

$$\tilde{F}_2 \equiv \frac{\partial \tilde{p}}{\partial \tilde{t}} + \gamma p_0 \frac{\partial \tilde{u}}{\partial \tilde{x}} + \zeta \frac{c_0}{L_0}\tilde{p} - (\gamma-1)\tilde{\dot{Q}}\tilde{\delta}_D(\tilde{x}-\tilde{x}_f) = 0. \tag{2.2}$$

The heat release is modelled with a form of King's law adapted by Balasubramanian & Sujith (2008*a*) from Heckl (1990). Surface heat transfer and subsequent thermal diffusion between the wire and the fluid are modelled by a constant time delay, $\tilde{\tau}$, between the time when the velocity acts and the time when the corresponding heat release is felt by the perturbation

$$\tilde{\dot{Q}} = \frac{2L_w(T_w-T_0)}{S\sqrt{3}}\left(\pi\lambda c_v \rho_0 \frac{d_w}{2}\right)^{1/2}\left(\left|\frac{u_0}{3}+\tilde{u}_f(\tilde{t}-\tilde{\tau})\right|^{1/2} - \left(\frac{u_0}{3}\right)^{1/2}\right), \tag{2.3}$$

where L_w, d_w and T_w represent the length, diameter and temperature of the wire, respectively, and S represents the cross-sectional area of the tube. This contains a time delay and a simple model for nonlinear attenuation, which are the two most influential characteristics in more sophisticated flame models (Dowling, 1997, 1999; Noiray *et al.* 2008).

2.2. *The non-dimensional governing equations*

Reference scales for speed, pressure, length and time are taken to be u_0, $p_0\gamma M$, L_0 and L_0/c_0, respectively. The inclusion of γM in the reference pressure differs from Balasubramanian & Sujith (2008*a*) but simplifies the subsequent analysis because the acoustic energy is then simply half the 2-norm of the state vector, as will be described in § 2.5. The dimensional variables, coordinates and Dirac delta can then be

written as

$$\tilde{u} = u_0 u, \quad \tilde{p} = p_0 \gamma M p, \quad \tilde{x} = L_0 x, \quad \tilde{t} = (L_0/c_0)t, \quad \tilde{\delta_D}(\tilde{x}-\tilde{x}_f) = \delta_D(x-x_f)/L_0, \tag{2.4}$$

where the quantities without a tilde or subscript 0 are dimensionless.

Substituting (2.4) into the dimensional governing equations (2.1) and (2.2) and making use of the definition of c_0 and the ideal gas law, $p_0 = \rho_0 R T_0$, gives the dimensionless governing equations

$$F_1 \equiv \frac{\partial u}{\partial t} + \frac{\partial p}{\partial x} = 0, \tag{2.5}$$

$$F_2 \equiv \frac{\partial p}{\partial t} + \frac{\partial u}{\partial x} + \zeta p - \beta \left(\left| \frac{1}{3} + u_f(t-\tau) \right|^{1/2} - \left(\frac{1}{3} \right)^{1/2} \right) \delta_D(x - x_f) = 0, \tag{2.6}$$

where

$$\beta \equiv \frac{1}{p_0 \sqrt{u_0}} \frac{(\gamma - 1)}{\gamma} \frac{2 L_w (T_w - T_0)}{S\sqrt{3}} \left(\pi \lambda c_v \rho_0 \frac{d_w}{2} \right)^{1/2}. \tag{2.7}$$

The system has four control parameters: ζ, which is the damping; β, which encapsulates all relevant information about the hot wire, base velocity and ambient conditions; τ, which is the time delay; and x_f, which is the position of the wire. The heat-release parameter, β, is equivalent to $k/\gamma M$ in Balasubramanian & Sujith (2008*a*).

2.3. *The boundary conditions and the discretized governing equations*

When appropriate boundary conditions in x are set, the governing equations (2.5) and (2.6) reduce to an initial value problem in t. For the system examined in this paper, $\partial u/\partial x$ and p are both set to zero at the ends of the tube. These boundary conditions are enforced by choosing basis sets that match these boundary conditions:

$$u(x,t) = \sum_{j=1}^{N} \eta_j(t) \cos(j\pi x), \tag{2.8}$$

$$p(x,t) = -\sum_{j=1}^{N} \left(\frac{\dot{\eta}_j(t)}{j\pi} \right) \sin(j\pi x), \tag{2.9}$$

where the relationship between η_j and $\dot{\eta}_j$ has not yet been specified. In this discretization, which is sometimes known as a Galerkin discretization, all the basis vectors are orthogonal.

The state of the system is given by the amplitudes of the Galerkin modes that represent velocity, η_j, and those that represent pressure, $\dot{\eta}_j/j\pi$. These are given the notation $\boldsymbol{u} \equiv (\eta_1, \ldots, \eta_N)^T$ and $\boldsymbol{p} \equiv (\dot{\eta}_1/\pi, \ldots, \dot{\eta}_N/N\pi)^T$. The state vector of the discretized system is the column vector $\boldsymbol{x} \equiv (\boldsymbol{u}; \boldsymbol{p})$.

The governing equations are discretized by substituting (2.8) and (2.9) into (2.5) and (2.6). As described in § 2.4, the damping, ζ, is dealt with by assigning a damping parameter, ζ_j, to each mode. Equation (2.6) is then multiplied by $\sin(k\pi x)$ and integrated over the domain $x = [0, 1]$. The governing equations then reduce to two delay differential equations (DDEs) for each mode, j:

$$F_{1G} \equiv \frac{\mathrm{d}}{\mathrm{d}t}\eta_j - j\pi \left(\frac{\dot{\eta}_j}{j\pi} \right) = 0, \tag{2.10}$$

$$F_{2G} \equiv \frac{\mathrm{d}}{\mathrm{d}t}\left(\frac{\dot{\eta}_j}{j\pi}\right) + j\pi\eta_j + \zeta_j\left(\frac{\dot{\eta}_j}{j\pi}\right)\cdots + 2\beta\left(\left|\frac{1}{3} + u_f(t-\tau)\right|^{1/2} - \left(\frac{1}{3}\right)^{1/2}\right)\sin(j\pi x_f) = 0, \quad (2.11)$$

where

$$u_f(t-\tau) = \sum_{k=1}^{N} \eta_k(t-\tau)\cos(k\pi x_f). \quad (2.12)$$

2.4. *Damping*

For the system examined in this paper, p and $\partial u/\partial x$ are both set to zero at the ends of the tube, which means that the system cannot dissipate acoustic energy by doing work on the surroundings. Furthermore, the acoustic waves are planar, which means that the system cannot dissipate acoustic energy in the viscous and thermal boundary layers at the tube walls. Both types of dissipation are modelled by the damping parameter for each mode:

$$\zeta_j = c_1 j^2 + c_2 j^{1/2}, \quad (2.13)$$

where c_1 and c_2 are the same for each mode. This model was used in Balasubramanian & Sujith (2008*a*) and Nagaraja *et al.* (2009) and was based on correlations developed by Matveev (2003) from models in Landau & Lifshitz (1959).

2.5. *The definition of the acoustic energy norm*

For the optimization procedure, it is necessary to define some measure of the size of the perturbations. Several measures are possible and each could give a different optimal. The most convenient measure is the acoustic energy per unit volume, $\tilde{E}$, because it is easy to calculate and has a simple physical interpretation (Nagaraja *et al.* 2009).

The acoustic energy per unit volume, $\tilde{E}$, consists of a kinetic component, $\tilde{E_k}$, and a pressure potential component, $\tilde{E_p}$. In dimensional form, it is given by

$$\tilde{E} = \tilde{E_k} + \tilde{E_p} = \frac{1}{2}\rho_0\left(\tilde{u}^2 + \frac{\tilde{p}^2}{\rho_0^2 c_0^2}\right). \quad (2.14)$$

Substituting for $\tilde{u}$ and $\tilde{p}$ from (2.4), making use of the ideal gas relation and defining the reference scale for energy per unit volume to be $\rho_0 u_0^2$, the dimensionless acoustic energy per unit volume, E, is given by

$$E = \frac{1}{2}u^2 + \frac{1}{2}p^2 = \frac{1}{2}\sum_{j=1}^{N}\eta_j^2 + \frac{1}{2}\sum_{j=1}^{N}\left(\frac{\dot{\eta}_j}{j\pi}\right)^2 = \frac{1}{2}\boldsymbol{x}^H\boldsymbol{x} = \frac{1}{2}\|\boldsymbol{x}\|^2, \quad (2.15)$$

where $\|\cdot\|$ represents the 2-norm. The rate of change of the acoustic energy with time is

$$\frac{\mathrm{d}E}{\mathrm{d}t} = u\frac{\mathrm{d}u}{\mathrm{d}t} + p\frac{\mathrm{d}p}{\mathrm{d}t} = \sum_{j=1}^{N}\eta_j\frac{\mathrm{d}\eta_j}{\mathrm{d}t} + \sum_{j=1}^{N}\left(\frac{\dot{\eta}_j}{j\pi}\right)\frac{\mathrm{d}}{\mathrm{d}t}\left(\frac{\dot{\eta}_j}{j\pi}\right) = -\sum_{j=1}^{N}\zeta_j\left(\frac{\dot{\eta}_j}{j\pi}\right)^2 - \sum_{j=1}^{N}2\beta\left(\frac{\dot{\eta}_j}{j\pi}\right)\left(\left|\frac{1}{3} + u_f(t-\tau)\right|^{1/2} - \left(\frac{1}{3}\right)^{1/2}\right)\sin(j\pi x_f). \quad (2.16)$$

The first term on the right-hand side of (2.16) represents damping and is always negative. The second term is the instantaneous value of $p\dot{Q}$ and is the rate at which thermal energy is transferred to acoustic energy at the wire. It is worth noting that this transfer of energy can be in either direction.

2.6. *The linearized governing equations*

Non-normality, which is central to this paper, is a linear phenomenon. It is most easily examined when the governing equations are linearized around $\boldsymbol{x}=0$ and expressed in the form $\mathrm{d}\boldsymbol{x}/\mathrm{d}t=\boldsymbol{L}\boldsymbol{x}$, where $\boldsymbol{x}$ represents the state of the system and $\boldsymbol{L}$ represents the evolution operator or matrix. Two linearizations are required to express the governing equations in this form. The first linearization, which is valid for $u_f(t-\tau)\ll 1/3$, is performed on the square-root term in (2.6) and (2.11):

$$\left(\left|\frac{1}{3}+u_f(t-\tau)\right|^{1/2}-\left(\frac{1}{3}\right)^{1/2}\right)\approx\frac{\sqrt{3}}{2}u_f(t-\tau). \tag{2.17}$$

This produces a system of linear DDEs: $\mathrm{d}\boldsymbol{x}/\mathrm{d}t=\boldsymbol{L}_1\boldsymbol{x}(t)+\boldsymbol{L}_2\boldsymbol{x}(t-\tau)$, where $\boldsymbol{L}_1$ is a normal matrix and $\boldsymbol{L}_2$ is a non-normal matrix. It is possible to find the eigenvalues of this linear DDE system (Selimefendigila, Sujith & Polifke 2010) and to quantify the non-normality of $\boldsymbol{L}_2$ but, in Balasubramanian & Sujith (2008*a*) and this paper, a second linearization is performed on the time delay:

$$\begin{aligned}u_f(t-\tau)&\approx u_f(t)-\tau\frac{\partial u_f(t)}{\partial t}\\&=\sum_{k=1}^{N}\eta_k(t)\cos(k\pi x_f)-\tau\sum_{k=1}^{N}k\pi\left(\frac{\dot{\eta}_k(t)}{k\pi}\right)\cos(k\pi x_f).\end{aligned} \tag{2.18}$$

This linearization is valid only for the Galerkin modes for which $\tau\ll T_j$, where $T_j=2/j$ is the period of the jth Galerkin mode. Equations (2.17) and (2.18) are substituted into (2.11) to give the linearized governing equations

$$F_{1G}\equiv\frac{\mathrm{d}}{\mathrm{d}t}\eta_j-j\pi\left(\frac{\dot{\eta}_j}{j\pi}\right)=0, \tag{2.19}$$

$$\begin{aligned}F_{2G}\equiv{}&\frac{\mathrm{d}}{\mathrm{d}t}\left(\frac{\dot{\eta}_j}{j\pi}\right)+j\pi\eta_j+\zeta_j\left(\frac{\dot{\eta}_j}{j\pi}\right)\cdots\\&+\sqrt{3}\beta s_j\sum_{k=1}^{N}\eta_k c_k-\sqrt{3}\beta\tau s_j\sum_{k=1}^{N}k\pi\left(\frac{\dot{\eta}_k}{k\pi}\right)c_k=0,\end{aligned} \tag{2.20}$$

where $s_j\equiv\sin(j\pi x_f)$ and $c_k\equiv\cos(k\pi x_f)$. This is a set of linear ordinary differential equations (ODEs), which can be expressed in the matrix form

$$\frac{\mathrm{d}}{\mathrm{d}t}\boldsymbol{x}=\frac{\mathrm{d}}{\mathrm{d}t}\begin{pmatrix}\boldsymbol{u}\\\boldsymbol{p}\end{pmatrix}=\begin{pmatrix}\boldsymbol{L}_{TL}&\boldsymbol{L}_{TR}\\\boldsymbol{L}_{BL}&\boldsymbol{L}_{BR}\end{pmatrix}\begin{pmatrix}\boldsymbol{u}\\\boldsymbol{p}\end{pmatrix}=\boldsymbol{L}\boldsymbol{x}. \tag{2.21}$$

The rate of change of energy $\mathrm{d}E/\mathrm{d}t$ can be found either by substituting (2.17) and (2.18) into (2.16) or by evaluating $\boldsymbol{x}^T\boldsymbol{L}\boldsymbol{x}$. This gives

$$\frac{\mathrm{d}E}{\mathrm{d}t}=-\sum_{j=1}^{N}\zeta_j\left(\frac{\dot{\eta}_j}{j\pi}\right)^2-\sqrt{3}\beta\sum_{j=1}^{N}\sum_{k=1}^{N}s_jc_k\left(\frac{\dot{\eta}_j}{j\pi}\right)\eta_k+\sqrt{3}\beta\tau\sum_{j=1}^{N}\sum_{k=1}^{N}s_jc_kk\pi\left(\frac{\dot{\eta}_j}{j\pi}\right)\left(\frac{\dot{\eta}_k}{k\pi}\right). \tag{2.22}$$

2.7. *The systems examined in this paper*

The thermoacoustic system examined in this paper has $x_f = 0.3$, $c_1 = 0.05$, $c_2 = 0.01$ and $\tau = 0.02$. These values are typical of a laboratory Rijke tube. (τ is slightly lower than that found in Heckl (1990), who used $\tau = 0.05$.) For the nonlinear results, the DDEs (see (2.10)–(2.11)) are integrated from $t = 0$. This requires information about u_f for $t \in [-\tau, 0)$ and adds as many degrees of freedom as there are time steps in this time period. In this paper, u_f is set to zero in this period in order to freeze these degrees of freedom. Although this is artificial, the effect is small because the time delay, $\tau = 0.02$, is very much smaller than the period over which transient growth takes place, which is of order 2–20.

One advantage of the Galerkin discretization is that concepts can be demonstrated on a small dimensional system and then readily extended to a large dimensional system. In this paper, the system is considered with 1, 3 and 10 Galerkin modes, labelled systems A, B and C, respectively. System A has two degrees of freedom and exhibits nonlinear characteristics but no non-normal transient growth over one cycle around the unstable periodic solution. System B has six degrees of freedom and exhibits both nonlinear and non-normal characteristics. System C is qualitatively identical to system B but has 20 degrees of freedom and is more representative of an actual thermoacoustic system.

For direct time marching, (2.10)–(2.11) are integrated with a fourth-order Runge–Kutta algorithm with $\delta t = 0.005$. For adjoint looping, the gradient information is found by integrating the equations in § B.6 with a first-order Euler algorithm with $\delta t = 0.00005$. These time steps are sufficiently small that the results are not sensitive to the time step.

3. The lower periodic solutions of the nonlinear governing equations

In § 7 it will be shown that there are two stable periodic solutions to the governing equations. The lower solution has velocity perturbations with amplitude less than the mean flow. The higher solution has velocity perturbations with amplitude greater than the mean flow. For simplicity, §§ 3–6 will consider only the lower solution, as if the higher solution did not exist. The higher solution will be introduced in § 7.

3.1. *The fixed point and periodic solutions on a bifurcation diagram*

The bifurcation diagrams for the system with 1, 3 and 10 Galerkin modes are shown in figure 1. These have been calculated with DDE Biftool (Engelborghs, Luzyanina & Roose 2002), which uses a continuation method similar to that described in Jahnke & Culick (1994). Each point on each line corresponds to a periodic solution. The top frames show the peak to peak amplitude of the first velocity mode, $\boldsymbol{u}_1$, as a function of the heat-release parameter, β, which is a standard representation. The bottom frames show the minimum acoustic energy on each periodic solution, for reasons that will be given in § 4.6. The influence of other bifurcation parameters, such as x_f, can be found in Subramanian *et al.* (2010).

The bifurcation diagrams are qualitatively similar to each other. At low values of β, there is a stable fixed point at zero amplitude. At the linear stability threshold, β_H, there is a subcritical Hopf bifurcation to an unstable periodic solution and an unstable fixed point. The unstable periodic solution becomes a stable periodic solution at a saddle node bifurcation at β_s. There are no other fixed points or periodic solutions (apart from the higher solution described in § 7). This is qualitatively similar to figure 6 of Ananthkrishnan *et al.* (2005), which is for a model with velocity-coupled nonlinear

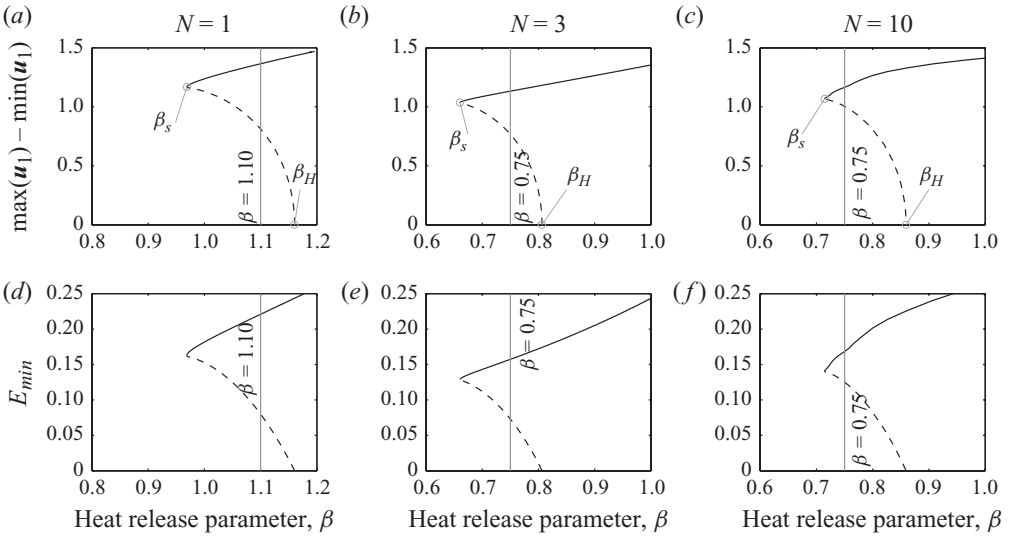

FIGURE 1. Bifurcation diagrams as a function of heat-release parameter, β, for the 1, 3 and 10 Galerkin mode systems (left to right). The top frames show the peak to peak amplitude of the first velocity mode. The bottom frames show the minimum acoustic energy on the periodic solutions. The solution with zero amplitude is stable up to $\beta = \beta_H$, where there is a Hopf bifurcation to an unstable periodic solution (dashed line). The unstable periodic solution becomes a stable periodic solution (solid line) at a saddle node bifurcation, β_s.

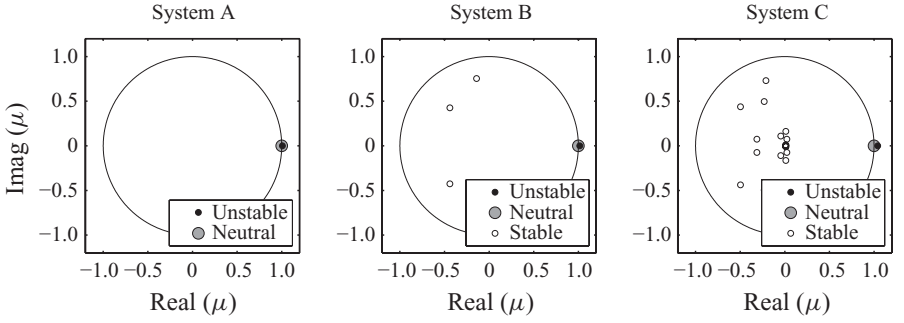

FIGURE 2. The Floquet multipliers, μ, of the unstable periodic solution for system A (which has $N = 1$, $\beta = 1.10$), system B (which has $N = 3$, $\beta = 0.75$) and system C (which has $N = 10$, $\beta = 0.75$). The unit circle is also shown. In each system, one Floquet multiplier is unstable ($|\mu| > 1$), one is neutral ($|\mu| = 1$), and, for systems B and C, the rest are stable ($|\mu| < 1$).

combustion and second-order gas dynamics. Between the saddle node bifurcation and the Hopf bifurcation, $\beta_s \leqslant \beta \leqslant \beta_H$, the system is susceptible to triggering. This configuration is also known as 'linearly stable but nonlinearly unstable' (Zinn & Lieuwen 2005).

For each periodic solution, the Floquet multipliers are calculated in order to determine whether it is stable (solid line) or unstable (dashed line). One Floquet multiplier is always equal to 1, corresponding to motion in the direction of the periodic solution, which neither grows nor decays over a cycle. For the stable periodic solution, all the other Floquet multipliers have magnitude less than 1, showing that this periodic solution attracts states from every other direction. For the unstable periodic solution, the Floquet multipliers are shown in figure 2. One Floquet multiplier

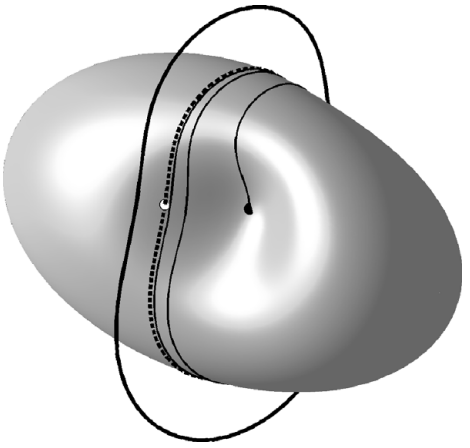

FIGURE 3. A cartoon of the boundary (grey surface) between the basins of attraction of the stable periodic solution (thick solid line) and the stable fixed point (not shown because it lies inside the surface). The unstable periodic solution (dashed line) is a closed loop on the basin boundary. This loop repels states away from the basin boundary, is neutral in the direction of the loop and attracts states in all other directions, as shown by the Floquet multipliers in figure 2. The most dangerous initial state (black dot) is the point with lowest energy infinitesimally outside the basin boundary. Its initial evolution (thin solid line) is towards the unstable periodic solution, closely following the basin boundary. From there, it is repelled towards the stable periodic solution. (This trajectory is not shown, to avoid complicating the figure.) If the system is non-normal, the most dangerous initial state (black dot) has lower energy than the point with lowest energy on the unstable periodic solution (white dot). In the cartoon, the basin boundary is shown as a two-dimensional surface but, in the model, it has dimension $2N-1$, where N is the number of Galerkin modes.

has absolute value greater than 1, one is neutral and the remainder have absolute value less than 1. This means that the unstable periodic solution (i) repels states in the direction of the eigenvector corresponding to the first Floquet multiplier, (ii) is neutral in the direction of the periodic solution and (iii) attracts states from every other direction.

3.2. *The basins of attraction of the stable solutions*

For β greater than β_H, all initial states evolve to the stable periodic solution. For β less than β_s, all initial states evolve to the stable fixed point. For β between these values, there is a boundary in state space between the basins of attraction of these two stable solutions. At β_H, this basin boundary is a surface enclosing an infinitesimally small volume around the stable fixed point. As β reduces, the volume inside the basin boundary increases until, at β_s, it contains all of state space. States outside the basin boundary evolve to the stable periodic solution. States within the basin boundary evolve to the stable fixed point. States exactly on the basin boundary stay on the boundary and, because there are no stable fixed points on the boundary, continually move around it. For illustration, we can think of this boundary as the surface of a potato, whose centre is the stable fixed point (figure 3). With the proviso about DDEs noted in § 2.7, the state space has dimension $2N$ and the basin boundary has dimension $2N-1$, where N is the number of Galerkin modes.

There is only one other closed loop in state space: the unstable periodic solution. Points exactly on the unstable periodic solution do not evolve to the stable fixed point or to the stable periodic solution because they lie on a loop. It is observed that

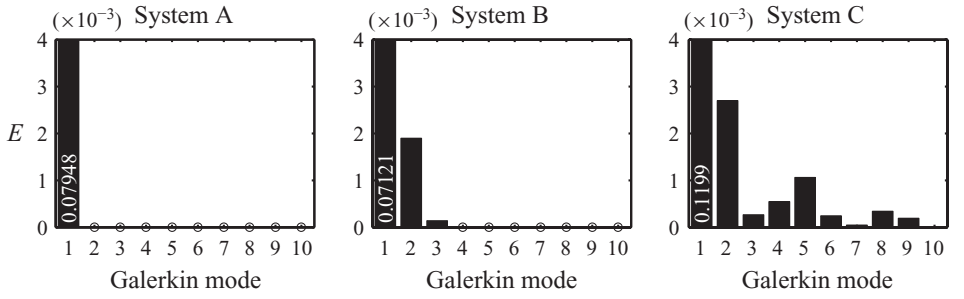

FIGURE 4. The distribution of energy in the Galerkin modes at the lowest energy point on the unstable periodic solution. The energy in the first mode, which greatly exceeds that in the other modes, is written on the first bar. The absolute values are significant because this is derived from a nonlinear analysis. The exact distribution of $\boldsymbol{u}$, $\boldsymbol{p}$ and E is in table 1.

neighbouring points evolve either to the stable periodic solution or to the stable fixed point. There are no other stable solutions in this region of state space. Therefore, the unstable periodic solution lies on the basin boundary. We can imagine the unstable periodic solution as a loop drawn on the surface of the potato (figure 3). This loop repels states away from the boundary, either towards the stable fixed point or towards the stable periodic solution, is neutral in the direction tangential to the loop, and attracts states in all other directions. Because there are no other periodic solutions or fixed points on the basin boundary, all points that start exactly on the basin boundary and near to the unstable periodic solution must be attracted towards the unstable periodic solution. This solution is known as an unstable attractor (Ashwin & Timme 2005), or a local relative attractor. We can think of these trajectories as lines drawn on the surface of the potato, spiralling towards the loop, without ever quite reaching it (figure 3).

Returning to the framework introduced in § 1.1, this basin boundary corresponds to the boundary that Skufca *et al.* (2006) call the 'edge of chaos' in fluid mechanics. The unstable periodic solution, which sits on the basin boundary, corresponds to the local relative attractor in Duguet *et al.* (2008) or, equivalently, the steady or quasi-steady periodic state identified in stage 3 of Schmid & Henningson (2001).

3.3. *Transient growth around the unstable periodic solutions of systems B and C*

One aim of this paper is to find the lowest energy initial state that just evolves to the stable periodic solution. This is equivalent to finding the lowest energy state on the basin boundary. The lowest energy state on the unstable periodic solution (figure 4 and table 1) is an obvious starting point because every state that starts exactly on the basin boundary evolves towards this periodic solution and must pass nearby. The question is now whether states can evolve towards the unstable periodic solution from lower energies than this state. In other words, what is the shape of the basin boundary around the unstable periodic solution? Is it convex or knobbly and does the lowest energy state on this loop lie at the bottom of a valley or on a slope?

To answer this, we will consider transient growth around the unstable periodic solution. Beforehand, it is worth reviewing studies that have looked at transient growth around the stable fixed point, such as Balasubramanian & Sujith (2008*a*). To do this, the governing equations are linearized around the fixed point (§ 2.6), and the linear stability operator, $\boldsymbol{L}$, is calculated (2.21). The eigenvalues of $\boldsymbol{L}$ describe the long time behaviour around the fixed point but, if the operator is non-normal,

		Galerkin mode number										
		1	2	3	4	5	6	7	8	9	10	Total
A	$\boldsymbol{u}$	−0.3986										
A	$\boldsymbol{p}$	0.0014										
A	E	0.0794										0.0794
B	$\boldsymbol{u}$	−0.3773	0.0615	0.0166								
B	$\boldsymbol{p}$	−0.0036	0.0034	0.0010								
B	E	0.0712	0.0018	0.0001								0.0732
C	$\boldsymbol{u}$	−0.4897	0.0734	0.0230	−0.0330	−0.0459	−0.0220	0.0097	0.0260	0.0195	0.0000	
C	$\boldsymbol{p}$	−0.0028	0.0036	0.0014	−0.0017	−0.0033	−0.0020	0.0007	0.0016	0.0009	0.0000	
C	E	0.1199	0.0027	0.0002	0.0005	0.0010	0.0002	0.0000	0.0003	0.0001	0.0000	0.1253

TABLE 1. Velocity amplitude, pressure amplitude and energy in each mode for the lowest energy points on the unstable periodic solution of systems A, B and C. The energy distribution is graphically shown in figure 4. The total energy is shown in the final column.

there can also be transient growth at intermediate times. This transient growth is particularly remarkable when all the eigenvalues are stable but is just as strong when some eigenvalues are unstable, e.g. figure 9 of Reddy & Henningson (1993). The perturbation that gives maximum transient energy growth over an arbitrary time, T, is the first left singular vector of $\exp(\boldsymbol{L}T)$. The maximum transient growth over all times is given the symbol G_{max} and occurs at time T_{max}. For system B, $G_{max} = 1.518$. For system C, $G_{max} = 1.588$. We will return to this in § 4. For more sophisticated models of thermoacoustic systems, $G_{max} \sim 10^6$ (Balasubramanian & Sujith 2008*b*).

A similar analysis can be applied around the unstable periodic solution (Schmid 2007; § 3.3). The governing equations are linearized around this periodic solution and the linear monodromy matrix, $\boldsymbol{M}$, is calculated, which describes the linear evolution of a perturbation over one cycle. The eigenvalues of this matrix, which are the Floquet multipliers, describe the behaviour around the periodic solution after many cycles. The singular values of this matrix describe the maximum possible growth over one cycle. If the monodromy matrix is non-normal, the largest singular value is larger than the largest eigenvalue, meaning that there is non-normal transient growth over one cycle. The perturbation that gives rise to the maximum possible growth over one cycle is the first singular vector of $\boldsymbol{M}$.

System A is a special case and is considered in § 3.4. For systems B and C, the monodromy matrices have been calculated numerically, starting from the lowest energy point on the unstable periodic solution. The eigenvalues of these matrices are the Floquet multipliers shown in figure 2 and the eigenvector corresponding to the largest Floquet multiplier is shown in figure 5 for both systems. For system B, the largest eigenvalue of $\boldsymbol{M}$ is 1.0136 and the largest singular value is 1.1657. For system C, the largest eigenvalue of $\boldsymbol{M}$ is 1.0422 and the largest singular value is 1.6058. For both systems, the largest singular value is greater than the largest eigenvalue, which means that there can be non-normal transient growth around the unstable periodic solution. The eigenvectors in figure 5 show the perturbation that grows fastest after many cycles. They have almost all their energy in the first mode. The first singular vectors in figure 6 show the perturbations that grow fastest after one cycle. They have most energy in the first, third and fourth modes (first and third for the three-mode system). For system C, this shows that the third and fourth modes are particularly influential in maximizing energy growth around the unstable periodic solution and

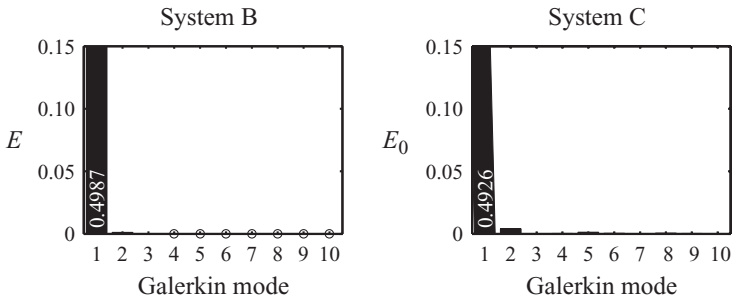

FIGURE 5. The distribution of energy in the Galerkin modes for the perturbation with maximum linear energy growth after many cycles around the unstable periodic solution. This is the eigenvector that corresponds to the largest eigenvalue of the monodromy matrix, which is the unstable Floquet multiplier in the corresponding frame of figure 2. The percentage energy in the first mode is 99.7 % for system B and 98.5 % for system C. The absolute value is not significant because this is derived from a linear analysis but, in these figures, the total energy is 0.5.

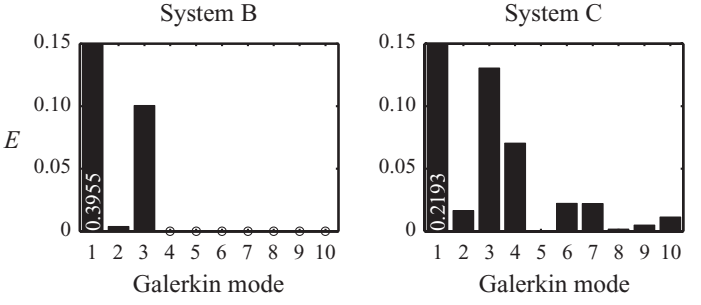

FIGURE 6. The distribution of energy in the Galerkin modes for the perturbation with maximum energy growth after one cycle around the unstable periodic solution. This is the first singular vector of the monodromy matrix. The percentage energy in the first mode is 79.1 % for system B and 43.9 % for system C. There is considerable energy in the higher modes. As for figure 5, the absolute value is not significant but, in these figures, the total energy is 0.5. The exact distribution of $\boldsymbol{u}$, $\boldsymbol{p}$ and E is in table 2.

that perturbation energy growth of $G_{cycle} = 1.6058^2 = 2.579$ can be achieved in the first cycle.

We can now determine whether states can evolve towards the lowest energy state on the unstable periodic solution from even lower energies. Exactly on the unstable periodic solution, there can be no transient energy growth over a cycle, by definition of a cycle. Adjacent to the unstable periodic solution, however, the energy of some trajectories grows transiently, i.e. faster than eigenvalue growth. Assuming that neighbouring trajectories are nearly parallel, this means that there must be a state that grows transiently during the first few cycles and is then attracted towards the unstable periodic solution. This state is on the basin boundary but has lower energy than the lowest energy state on the unstable periodic solution. The linear techniques using the monodromy matrix suggest that these states will be found by adding some amplitude of the singular vectors in figure 6 to the lowest energy points on the respective unstable periodic solutions in figure 4. The nonlinear techniques in § 4 find this state exactly.

	Galerkin mode number										
	1	2	3	4	5	6	7	8	9	10	Total
B $\boldsymbol{u}$	−0.5074	−0.0787	−0.0910								
B $\boldsymbol{p}$	0.7303	0.0402	0.4392								
B E	0.3954	0.0039	0.1006								0.5
C $\boldsymbol{u}$	−0.4461	−0.0028	0.1027	0.1676	0.0186	−0.0625	−0.0501	−0.0113	0.0179	0.0264	
C $\boldsymbol{p}$	0.4895	0.1821	0.5004	0.3360	−0.0228	−0.2018	−0.2042	−0.0587	0.0980	0.1487	
C E	0.2193	0.0165	0.1305	0.0705	0.0004	0.0223	0.0221	0.0017	0.0049	0.0114	0.5

TABLE 2. Velocity amplitude, pressure amplitude and energy in each mode for the SVD of the monodromy matrix on the unstable periodic solution of systems B and C. The energy distribution is shown graphically in figure 6. The total energy is not significant because these results are derived from a linear analysis.

3.4. *The special case of system A*

System A is a special case. With the proviso about DDEs noted in § 2.7, system A has only two degrees of freedom: $\boldsymbol{u}_1$ and $\boldsymbol{p}_1$. Its periodic solutions are one-dimensional loops in two-dimensional state space. This means that the unstable periodic solution is equivalent to the basin boundary between the stable fixed point and the stable periodic solution. States must either decay towards the fixed point or towards the stable periodic solution. Although the energy of states can grow transiently within a cycle if the basin boundary is elliptic, they cannot grow transiently over one or more cycles and then subsequently decay because, if they did, trajectories in state space would cross, which is forbidden. This is why Noiray *et al.* (2008), who froze the harmonics to the fundamental mode, could not have predicted transient growth. For a system to have transient growth, the harmonics must be free to evolve independently. It must be stressed that the equivalence between the unstable periodic solution and the basin boundary arises only because system A has two degrees of freedom. Systems B and C, which have more degrees of freedom, are qualitatively different (Strogatz 2001; § 6.2).

4. Calculation of linear and nonlinear optimal initial states

This section describes a process that finds the initial state that is attracted to the unstable periodic solution from the lowest initial energy. This state is an infinitesimal distance from the lowest energy point on the basin boundary in § 3.2 and is labelled the 'most dangerous' initial state. In § 3, we saw that the unstable periodic solution lies on the basin boundary of the stable periodic solution and, in systems B and C, that it repels states in one direction, is neutral in one direction and attracts states in all other directions. We saw that the monodromy matrix is non-normal, meaning that linear transient growth around the unstable periodic solution is possible. The linear analysis is, however, valid only in a small region around the unstable periodic solution, and therefore, does not provide a systematic way to find the most dangerous initial state of the nonlinear governing equations. In this section, we will start by considering linear optimal states around the stable fixed point and then move on to a more general definition of nonlinear optimal states, from which a process is developed to find the most dangerous initial state.

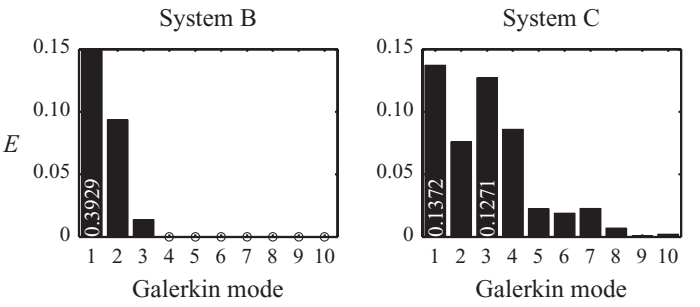

FIGURE 7. The distribution of energy in the Galerkin modes for the perturbation with maximum energy growth around the stable fixed point. This is the first singular vector of the stability matrix $\boldsymbol{L}$. As for figure 5, the absolute value is not significant but, in these figures, the total energy is 0.5.

4.1. *Linear and nonlinear optimization procedures*

Of all the possible initial states, $\boldsymbol{x}_0$, one will give the maximum acoustic energy growth, $G(T)$, over some arbitrary time T. This is defined as

$$G(T) = \max_{\boldsymbol{x}_0} \frac{\|\boldsymbol{x}(T)\|^2}{\|\boldsymbol{x}_0\|^2}. \tag{4.1}$$

The optimal $\boldsymbol{x}_0(T)$ and corresponding $G(T)$ can be found with an optimization routine. For the linear system, however, there is a simpler method: $G(T)$ is the square of the highest singular value of $\exp(\boldsymbol{L}T)$ and the optimal $\boldsymbol{x}_0(T)$ is the first left singular vector of $\exp(\boldsymbol{L}T)$, where $\boldsymbol{L}$ is the matrix that represents the linearized governing equations (cf. (2.21)) (Schmid 2007). In a further optimization, $G(T)$ can be optimized over all T. This is denoted by G_{max} and occurs at time T_{max}. The corresponding initial state is called the linear optimal initial state around the stable fixed point. This is shown in figure 7 for systems B and C. It is interesting to note the high amplitudes of the third and fourth modes in system C, a characteristic shared by the optimal initial perturbation around the unstable periodic solution shown in figure 6.

For the linear system, the direction of $\boldsymbol{x}_0$ is influential but its magnitude is not. For the nonlinear system, however, both the direction and the magnitude of $\boldsymbol{x}_0$ are influential. If the magnitude of x_0 is quantified by its energy, E_0, then G in (4.1) becomes a function of T and E_0. The singular value decomposition (SVD) cannot be applied to nonlinear systems and also requires cost functionals to be expressed as 2-norms. To find $G(T, E0)$ or to investigate more elaborate cost functionals, a new technique is required.

The technique used in this paper is adapted from optimal control (Bewley 2001). In brief, a cost functional, $\mathfrak{J}$, is defined, which may or may not be $\|\boldsymbol{x}(T)\|^2/\|\boldsymbol{x}_0\|^2$. A Lagrangian functional, $\mathfrak{L}$, is then defined as the cost functional, $\mathfrak{J}$, minus a set of inner products. These inner products multiply the governing equations by one set of Lagrange multipliers and the initial state by another set of Lagrange multipliers. When all variations of $\mathfrak{L}$ with respect to the Lagrange multipliers, state variables, $\boldsymbol{x}$, and initial state, $\boldsymbol{x}_0$, are zero, an initial state has been found that optimizes $\mathfrak{J}$ and satisfies the governing equations.

To find this initial state, the direct governing equations are integrated forward for time T from an initial guess, thus satisfying the requirement that all variations of $\mathfrak{L}$ with respect to the Lagrange multipliers are zero. The Lagrangian functional is then re-arranged so that it is expressed in terms of a different set of inner products. These

inner products multiply the state variables, $\boldsymbol{x}$, by a first set of constraints. They also multiply the initial state, $\boldsymbol{x}_0$, by a second set of constraints. The requirement that all variations of $\mathfrak{L}$ with respect to $\boldsymbol{x}$ are zero can be met by satisfying the first constraints. Half of these, known as the *optimality conditions*, determine the relationship between an adjoint state vector, $\boldsymbol{x}^+$, and the direct state vector, $\boldsymbol{x}$, at time T. The other half, known as the *adjoint* governing equations, govern the evolution of $\boldsymbol{x}^+$ for $t=[0,T]$. After setting the optimality conditions at $t=T$, the adjoint governing equations are integrated backwards to time 0, thus satisfying the requirement that all variations of $\mathfrak{L}$ with respect to $\boldsymbol{x}$ are zero. The second set of constraints return the gradient information $\partial\mathfrak{L}/\partial\boldsymbol{x}_0$ at the initial guess for $\boldsymbol{x}_0$. This is combined with a convenient optimization algorithm, such as the steepest descent method or the conjugate gradient method, in order to converge towards the optimal initial state, at which $\partial\mathfrak{L}/\partial\boldsymbol{x}_0=0$.

This technique is extremely versatile. It can handle all reasonable cost functionals, boundary conditions and governing equations, either linear or nonlinear. It also allows accuracy to be traded for speed by reducing the temporal resolution or the tolerance of the optimization. The adjoint governing equations, optimality conditions and gradient information are derived for the nonlinear case with cost functional $\mathfrak{J}_{av}$ in Appendix A. For the other cases, these equations are listed without derivation in Appendix B.

4.2. *The characteristics of different cost functionals*

Several cost functionals would be appropriate for the optimization in this paper, each with slightly different adjoint equations. One is the final energy divided by the initial energy, $\mathfrak{J}_T\equiv E(T)/E_0$, which is equal to G at optimality. Another is the integrated rate of energy transfer between the thermal and the mechanical field, $\mathfrak{J}_{pQ}\equiv\int_0^T p\dot{Q}\,\mathrm{d}t$, which is equivalent to $\mathfrak{J}_T$ without including damping. Both of these oscillate with time. Another is the average energy over some specified time window, which also oscillates unless the time window happens to be exactly equal to one period. Given that the solution becomes periodic only once the transient behaviour has died away and that the period is not necessarily known beforehand, the oscillations cannot, in general, be removed by using this cost functional. Another is the average acoustic energy over $t=[0,T]$ divided by the initial energy: $\mathfrak{J}_{av}\equiv E_{av}(T)/E_0$. This cost functional increases monotonically with time, which is sometimes a useful feature. The cost functionals $\mathfrak{J}_T$ and $\mathfrak{J}_{av}$ are used in this paper.

4.3. *Local optimization of the nonlinear governing equations*

The local optimization procedure consists of an adjoint looping algorithm and a line maximization algorithm nested within a conjugate gradient algorithm. The adjoint looping algorithm provides gradient information to the conjugate gradient algorithm. This procedure finds local maxima of $\mathfrak{J}$ from an initial guess for $\boldsymbol{x}_0$. Two versions of the procedure are used. In the first version, no constraints are placed on the initial state. In the second version, the energy of the initial state, E_0, is specified. The second version (or some variant of it) is required when the linear governing equations are being optimized so that the solution does not grow to infinity or decay to zero. Although the initial energy is irrelevant to the linear solution, allowing it to grow or decay without constraint can lead to numerical problems. The second version is also useful in the global optimization procedures described in § 4.5.

4.3.1. *The conjugate gradient algorithm*

Step 1: Starting from an initial guess for $\boldsymbol{x}_0$, the gradient $\partial\mathfrak{J}/\partial\boldsymbol{x}_0$ at that point is calculated via the adjoint looping algorithm in § 4.3.2. The direction of steepest ascent of $\mathfrak{J}$ is supplied to step 2.

Step 2: The initial state $\boldsymbol{x}_0$ is incremented by $\delta\boldsymbol{x}_0$ in the given direction until a maximum is reached. The maximum along this path is found accurately with a line maximization routine that assumes that the peak is locally parabolic. This requires several integrations of the governing equations but no integration of the adjoint governing equations. If the initial energy has been specified, then this path is constrained to the surface of the $2N$-dimensional sphere with radius $\sqrt{2E_0}$.

Step 3: Step 1 is repeated to find the direction of steepest ascent of $\mathfrak{J}$ at the new initial state.

Step 4: A new direction is calculated with the conjugate gradient algorithm (Press *et al.* 1992). This is usually close to the line of steepest ascent of $\mathfrak{J}$ but uses information about the previous direction in order to avoid zig-zagging, particularly along ridges.

Step 5: Steps 2–4 are repeated until the initial state $\boldsymbol{x}_0$ has converged sufficiently closely to a local maximum of $\mathfrak{J}$.

Step 6: The exact maximum is found to a greater tolerance by carrying out the parabolic convergence of step 2 for each component of $\boldsymbol{x}_0$.

4.3.2. *The adjoint looping algorithm*

Step 1: Starting from an initial state, $\boldsymbol{x}_0$, the discretized governing equations (§ B.3) are integrated forward for the required time, T, with a first-order Euler or fourth-order Runge–Kutta algorithm with constant time step δt. At each time step, the state, $\boldsymbol{x}(t)$, and all the intermediate variables are stored for use during the backward integration with the adjoint governing equations.

Step 2: At $t = T$, the optimality conditions (§ B.7) are applied, which initializes the adjoint variables at $t = T$.

Step 3: The discretized adjoint governing equations (§ B.6) are integrated backwards to $t = 0$ with an algorithm identical to that in step 1. This uses the state and the intermediate variables that were stored during the forward calculation.

Step 4: The gradients of $\mathfrak{J}$ with respect to the initial conditions, $\partial\mathfrak{J}/\partial\boldsymbol{x}_0$, are calculated (§ B.8). This gives the direction of steepest ascent of $\mathfrak{J}$, which is returned to the conjugate gradient algorithm.

4.4. *A demonstration of the local optimization procedure*

The horizontal Rijke tube with one Galerkin mode is a convenient system on which to demonstrate the optimization procedure because its two degrees of freedom can be represented on a plane. Figure 8(*a*) shows contours of $\mathfrak{J}_T$ as a function of $(\boldsymbol{u}_1, \boldsymbol{p}_1)$ for system A evolving to $T = 2$ with the linearized governing equations. The arrows show the gradient calculated with the adjoint looping algorithm in § 4.3.2, and it is easy to check that these lie perpendicular to the contours of $\mathfrak{J}$.

The white dot is the starting point for the optimization process and the small black dots are the steps taken during the line maximization process. In this case (figure 8*a*), E_0 has been constrained; so all these points lie on the white circle. The optimal point $\boldsymbol{x}_{0_{max}}$ is given by the big black dot and is identical to the SVD solution, which is given by the black line. In the linear case, the amplitude is irrelevant, which means that the contours of constant $\mathfrak{J}$ are straight lines radiating from $\boldsymbol{x}_0 = 0$. This also means that $\mathfrak{J}$ at $\boldsymbol{x}_{0_{max}}$ is equal to $\mathfrak{J}$ at $-\boldsymbol{x}_{0_{max}}$, which becomes useful in § 4.5.

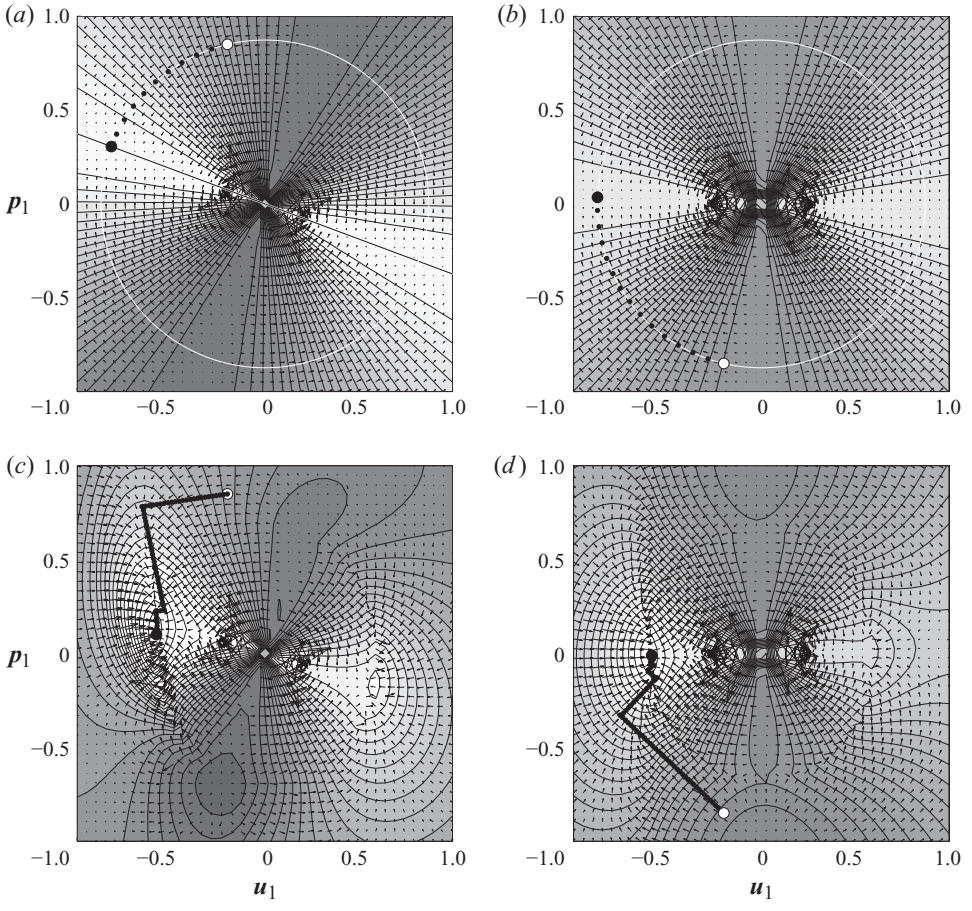

FIGURE 8. Contours of cost functional, $\mathfrak{J}(\boldsymbol{u}_1, \boldsymbol{p}_1)$, for system A for: (*a*) $\mathfrak{J} = \mathfrak{J}_T$ evolving to $T = 2$ with the linear governing equations; (*b*) $\mathfrak{J} = \mathfrak{J}_{av}$ evolving to $T = 2$ with the linear governing equations; (*c*) $\mathfrak{J} = \mathfrak{J}_T$ evolving to $T = 2$ with the nonlinear governing equations; (*d*) $\mathfrak{J} = \mathfrak{J}_{av}$ evolving to $T = 2$ with the nonlinear governing equations. The arrows show the gradients calculated with the adjoint looping algorithm in § 4.3.2. The path of the optimization process described in § 4.3.1 is shown from the initial guess (white dot) to the optimal point (big black dot). In (*a*) and (*b*) the initial energy is fixed. In (*c*) and (*d*) it is unconstrained.

The optimal point can be found to any specified tolerance, although there is a trade-off between the time taken and the accuracy. In the Rijke tube system, for which the linear governing equations can be represented by a small matrix (e.g. 20×20 for system C), the SVD method is around three orders of magnitude faster than the adjoint looping method. In systems that are represented by a large matrix (greater than 1000×1000), such as that studied by Balasubramanian & Sujith (2008*b*), the adjoint looping method is faster than the SVD method.

The remaining frames of figure 8 show the same information for (*b*) cost functional $\mathfrak{J}_{av}$ with the linearized governing equations, (*c*) cost functional $\mathfrak{J}_T$ with the nonlinear governing equations for unconstrained E_0 and (*d*) cost functional $\mathfrak{J}_{av}$ with the nonlinear governing equations for unconstrained E_0. The linear cases are qualitatively similar to each other, showing that both cases have unique optimal starting points, $\boldsymbol{x}_{0_{max}}$, whether the cost functional be $\mathfrak{J}_T$, which can be analysed with the SVD method,

or $\mathfrak{J}_{av}$, which cannot. The nonlinear cases are also qualitatively similar to each other but do not have the simple structure of the linear cases. In particular, they each have two local maxima, the consequences of which will be discussed in § 4.5.

4.5. *Global optimization of the nonlinear governing equations*

The conjugate gradient algorithm combined with line maximization and adjoint looping is an efficient way to find local maxima of $\mathfrak{J}$. In the linear case, there is a single maximum. In the nonlinear case, however, there are several local maxima. This can be seen in figures 8(*c*) and 8(*d*) for system A. In systems B and C, there are many more local maxima.

In this paper, the global maximum is found with a simulated annealing process. Once a local maximum has been found, random perturbations are added to the state vector and new local maxima are sought from these points. Most of these converge to the original local maximum but, occasionally, a new local maximum is found in a new area. This process continues, with progressively smaller random perturbations until the global maximum is found. The simulated annealing process is robust but slow, and it is highly likely that a more efficient global optimization procedure can be found.

4.6. *Efficient convergence to the most dangerous initial state*

The global optimization procedure in § 4.5 can find the initial states with maximum possible transient growth, $G(T, E_0)$, over a wide range of T and E_0 (Juniper 2010). The aim of the current paper, however, is to find the state with the lowest initial energy, E_0, that can reach sustained oscillations. This is the state with lowest energy on the basin of attraction of the stable periodic solution. This point can be found by using the global optimization procedure with cost functional $\mathfrak{J}_T = E(T)/E_0$ over a long time window with unconstrained E_0 but this is time-consuming (Juniper & Waugh 2010).

A different procedure is used here. We know from § 3 that all states very close to the basin boundary start by evolving towards the unstable periodic solution. This means that the optimization needs to be performed only on the first few time units, during which transient growth to the unstable periodic solution takes place. After this period, the evolution from all initial states near the boundary is similar. An optimization time of $T = 10$ has been found to be sufficient but $T = 20$ is used in this paper, corresponding to 10 periods of the first mode's natural frequency. If the optimization period is too short, the initial state with highest transient growth can be one that subsequently decays very quickly.

The optimization procedure starts from the lowest energy point on the unstable periodic solution because this is the lowest energy point on the basin boundary that can be found with the continuation method. There is no transient growth around the cycle when starting from this point. The global optimization process then finds a state that has the same initial energy but that maximizes transient growth over 20 time units. Its amplitude is then reduced incrementally and the evolution calculated well beyond the period of transient growth. This is repeated until the initial energy is found at which the state evolves to the unstable periodic solution but then neither grows nor decays over several hundred time units. This point is extremely close to the basin of attraction of the stable periodic solution and has lower energy than the previous point but is not necessarily the most dangerous initial state. The optimization process

	Galerkin mode number										
	1	2	3	4	5	6	7	8	9	10	Total
B $\boldsymbol{u}$	−0.3715	−0.0040	−0.0331								
B $\boldsymbol{p}$	−0.0356	0.0112	0.0005								
B E	0.0696	0.0001	0.0005								0.0702
C $\boldsymbol{u}$	−0.4334	−0.0321	−0.1298	−0.0596	−0.0009	−0.0035	0.0146	0.0063	0.0025	0.0301	
C $\boldsymbol{p}$	−0.0813	0.0191	0.0021	−0.0353	−0.0004	−0.0025	0.0006	0.0072	−0.0178	−0.0101	
C E	0.0972	0.0007	0.0084	0.0024	0.0000	0.0000	0.0001	0.0000	0.0001	0.0005	0.1096

TABLE 3. Velocity amplitude, pressure amplitude and energy in each mode for the most dangerous initial state of systems B and C. The energy, E, is shown graphically in figure 9. The total energy is shown in the final column. It is significantly lower than the energy of the lowest energy point on the unstable periodic solution in table 1.

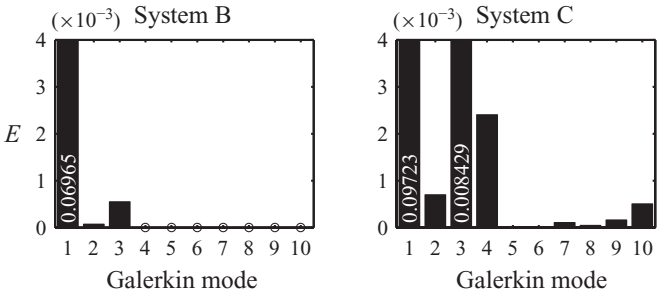

FIGURE 9. The distribution of energy in the Galerkin modes for the most dangerous initial states for systems B and C, found with the optimization procedure in § 4. The absolute values are significant because this is derived from a nonlinear analysis. The exact distribution of $\boldsymbol{u}$, $\boldsymbol{p}$ and E is in table 3. These states lie just within the basin of attraction of the stable periodic solution. As expected from the first singular value of the monodromy matrix in figure 6, system B has significant energy in the third mode and system C has significant energy in the third and fourth modes in order that these initial states can maximize their energy growth around the unstable periodic solution.

and the energy reduction process are repeated in sequence until any further reduction in the energy is less than 10^{-4}.

5. Transient growth and triggering from the most dangerous initial state

The procedure in § 4 is used to find the most dangerous initial states for systems B and C. These initial states are shown in figure 9 and table 3. The evolution from them is shown in figures 10 and 11, in which frames (*a*) and (*b*) show the same data on different time scales. In both systems, the most dangerous state grows transiently around the unstable periodic solution for a few cycles, and then follows the unstable periodic solution for a few hundred time units before growing towards the stable periodic solution. Although not shown here, if the amplitude of the initial state is reduced very slightly, it evolves along a neighbouring trajectory but then decays to the zero solution. This is qualitatively identical to, but much simpler than, the process seen in bypass transition to turbulence described in § 1.1.

The question now arises as to whether this transient growth towards the unstable periodic solution arises due to non-normality. In hydrodynamics, this is simple to

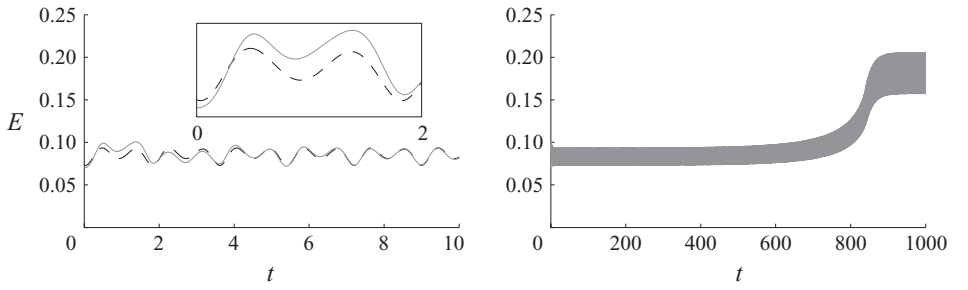

FIGURE 10. Evolution with the nonlinear governing equations from the most dangerous initial state of system B (grey line). The energy of the system grows transiently over the first few cycles, then follows the unstable periodic solution (dashed line) for several cycles, before growing to the stable periodic solution.

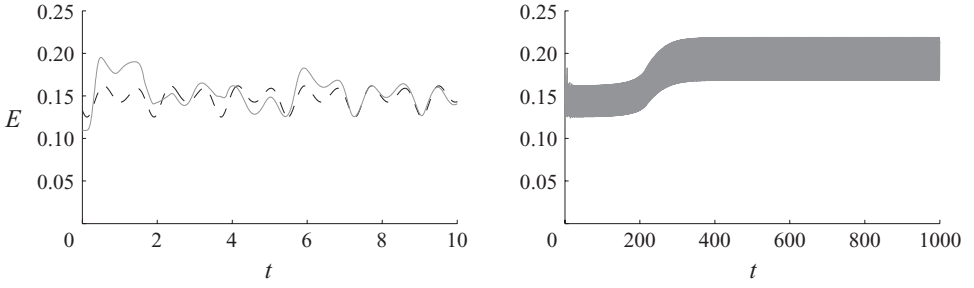

FIGURE 11. As for figure 10 but for system C. The transient growth is stronger in system C. Although this state evolves to the stable periodic solution earlier than system B, this is not significant because the time spent around the unstable periodic solution is extremely sensitive to tiny variations in the amplitude of the initial state.

answer because the nonlinear terms conserve energy, meaning that any energy growth must be due to linear terms and, if all eigenvalues are linearly stable, must therefore be due to non-normality. In thermoacoustics, however, the nonlinearity does not conserve energy and could cause transient growth even in the absence of non-normality.

We know, however, from § 3.3 that the monodromy matrix of the unstable periodic solution is non-normal and that this causes linear transient growth around the unstable periodic solution. Furthermore, the linear perturbations that cause the highest transient energy growth have highest amplitudes in the first, third and fourth modes (in the first and third modes for system B). This characteristic is shared by the nonlinear most dangerous initial states. This strongly suggests that transient growth in the nonlinear system is also due to linear non-normality. Further evidence is provided in figure 12. This shows the evolution from the most dangerous initial state for system C, using the governing equations linearized around the stable fixed point (see (2.19)–(2.20)). The first point to note, by comparing this linear evolution with the unstable periodic solution (dashed line), is that the initial energy growth of the linear evolution exceeds that of the unstable periodic solution. Put together with the results from the monodromy matrix, this shows that transient growth arises from the linear part of the evolution operator, whether this operator is linearized about the stable fixed point or around the unstable periodic solution. The second point to note, by comparing the linear evolution (solid line in figure 12) with the nonlinear evolution (solid line in figure 11), is that the nonlinear system has larger transient

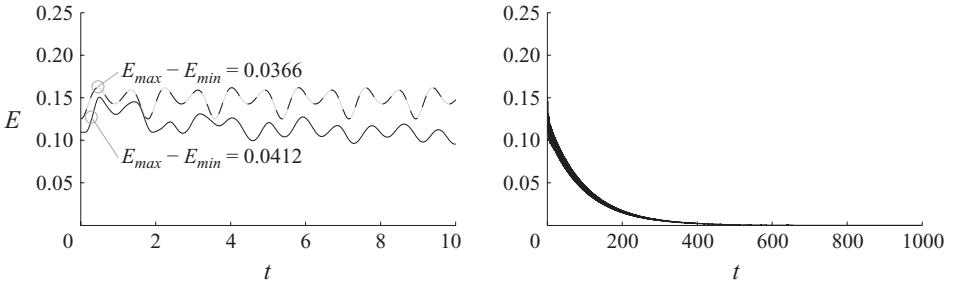

FIGURE 12. Evolution with the linear governing equations from the optimal initial point of system C (black line), showing transient growth at the very beginning but then decay to the stable fixed point at zero, which is the only solution of the linear governing equations. This shows that the linear transient growth from this point exceeds that which is achieved from starting at the minimum energy point of the unstable periodic solution (dashed line).

growth than the linear system. This shows that, around the unstable periodic solution, both nonlinearity and non-normality contribute to transient growth. The same result has been found for transient growth around the stable fixed point (Juniper 2010). On this feature, thermoacoustic systems differ from hydrodynamic systems.

It is worth pointing out that the linear optimal state around the stable fixed point, shown in figure 7, differs significantly from the most dangerous initial state. Although, for system C, both have high energies in the third and fourth modes, the most dangerous initial state has much higher energy in the first mode in order for it to start near the unstable periodic solution. At the energies required for triggering, the linear optimal around the stable fixed point has little transient growth. This is described in detail in Juniper (2010).

In summary, the most dangerous initial state has been found by embedding nonlinear adjoint looping within a conjugate gradient algorithm. This is a brute force approach that makes no assumptions about the mechanisms of transient growth. It is seen that this initial state exploits linear transient growth around the unstable periodic solution in order to be attracted initially towards the unstable periodic solution and, from there, towards the stable periodic solution. This is directly analogous to stages 2–4 in bypass transition to turbulence (§ 1.1). There are, however, some differences between triggering in thermoacoustics and bypass transition in hydrodynamics. Firstly, nonlinearity (as well as non-normality) contributes to transient growth in thermoacoustics. Secondly, at least in this simple thermoacoustic model, the basin boundary contains only one unstable periodic solution while, in hydrodynamics, it contains several.

6. The 'safe operating region' of this model

In an industrial situation, it would be acceptable to operate a system that is 'linearly stable but nonlinearly unstable' as long as the system could never be perturbed sufficiently to reach the stable periodic solution. The most dangerous initial states give the upper bound of this 'safe operating region'. These have been calculated at several values of β for systems B and C. The results are shown in figure 13. This shows the lowest energy on the unstable periodic solution (dashed line), the lowest energy on the stable periodic solution (solid line) and the energy of the most dangerous initial states (dotted line). (For system A, the dotted line would coincide with the dashed

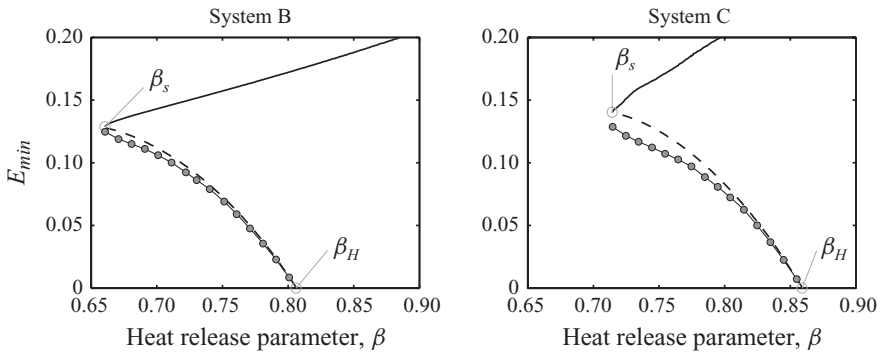

FIGURE 13. The minimum energy on the stable periodic solution (solid line) and unstable periodic solution (dashed line) for systems B and C. The dotted line corresponds to the energy of the most dangerous initial states, found with the optimization procedure. These states reach the stable periodic solution. The region below the dotted line and to the left of β_s corresponds to the 'safe' operating region of the Rijke tube. It is smaller than that which would be predicted from a nonlinear but normal analysis.

line in figure 1(a) because the most dangerous initial state is equivalent to the lowest energy point on the unstable periodic solution.)

In system B, the most dangerous initial states can have up to 5.4 % less energy than the lowest energy on the unstable periodic solution. For comparison, typical values (calculated at $\beta = 0.75$) for linear transient growth of this system are $G_{max} = 1.518$ when linearized around the stable fixed point and $G_{cycle} = 1.359$ when linearized around the unstable periodic solution. In system C, the most dangerous initial states have up to 12.5 % lower energy than the unstable periodic solution. Typical values are $G_{max} = 1.588$ and $G_{cycle} = 2.579$ at $\beta = 0.75$. The values of G_{max} and G_{cycle} give a rough indication of the gap between the dashed and dotted lines in figure 13. For more elaborate thermoacoustic models, such as that in Balasubramanian & Sujith (2008*b*), G_{max} is of order 10^6 and G_{cycle} has yet to be determined. It is likely that the most dangerous initial states of these systems will have significantly lower energy than that on the unstable periodic solution.

A linear analysis would predict the safe operating region to be all regions to the left of β_H. A nonlinear but normal analysis, such as Noiray *et al.* (2008), would predict the safe operating region to be all regions to the left of β_s and all regions below the lowest energy on the unstable periodic solution (dashed line) between β_s and β_H. The nonlinear and non-normal analysis in this paper shows that the safe operating region between β_s and β_H is smaller than that predicted by a normal analysis. A nonlinear and non-normal analysis of more elaborate thermoacoustic systems, which have higher linear transient growth, is likely to reveal that the safe operating region between β_s and β_H is even smaller.

7. The higher periodic solutions of the nonlinear governing equations

The periodic solutions presented so far correspond to perturbation velocities that have smaller magnitude than the mean flow. This means that the net flow is always in the downstream direction. The system can also support periodic solutions with perturbation velocities that have larger magnitude than the mean flow. This means that the net flow can reverse. The model in this paper does not support nonlinear

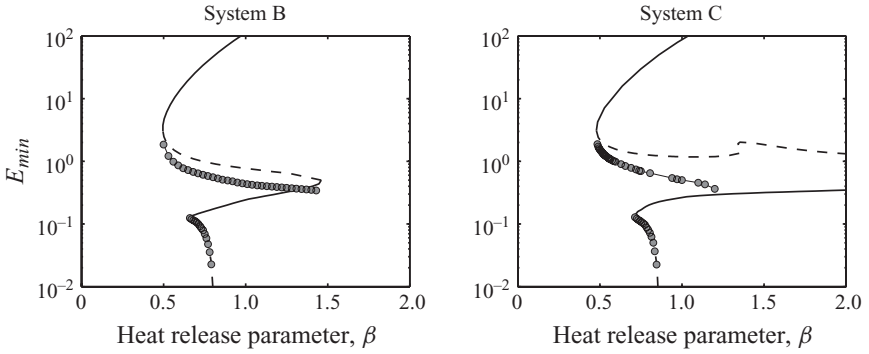

FIGURE 14. The minimum energy on the stable periodic solution (solid lines) and unstable periodic solution (dashed lines) for systems B and C. The dotted lines correspond to the energy of the most dangerous initial states, found with the optimization procedure. These states reach the stable periodic solution above them.

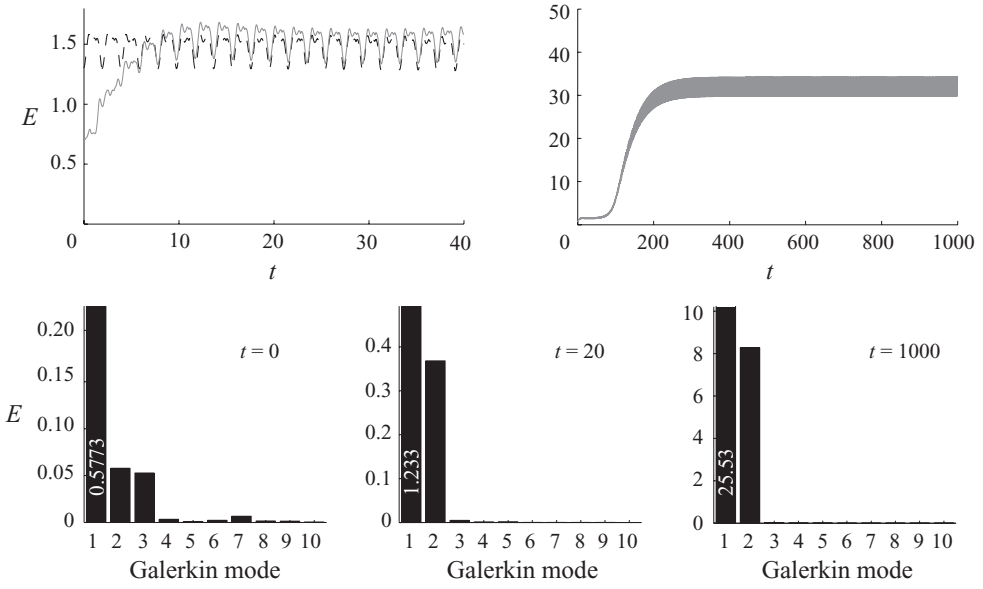

FIGURE 15. As for figure 10 but for the higher periodic solutions of system B. The distribution of energy in the Galerkin modes is shown at the start ($t = 0$), on the upper unstable periodic solution ($t = 20$ and dashed line) and on the upper stable periodic solution ($t = 1000$). On the bar charts, the vertical axes are scaled to 25 % of the amplitude of the first mode.

acoustics, which may well be influential in this range. Nevertheless, these results are worth reporting, even if they are only qualitatively correct.

The second pair of periodic solutions, one unstable and one stable, are shown in figure 14 for systems B and C. Log scales are used because the energy is much higher than that of the first pair of periodic solutions. The most dangerous initial states that can reach these periodic solutions (dotted line) lie at significantly lower energy than that of the unstable periodic solution. Figures 15 and 16 show time evolutions from the most dangerous initial conditions at $\beta = 0.75$. They start from low energies ($E_0 = 0.6013$ for system C and $E_0 = 0.7026$ for system C), grow transiently over 5–10 time units, are attracted towards the unstable periodic solutions for around

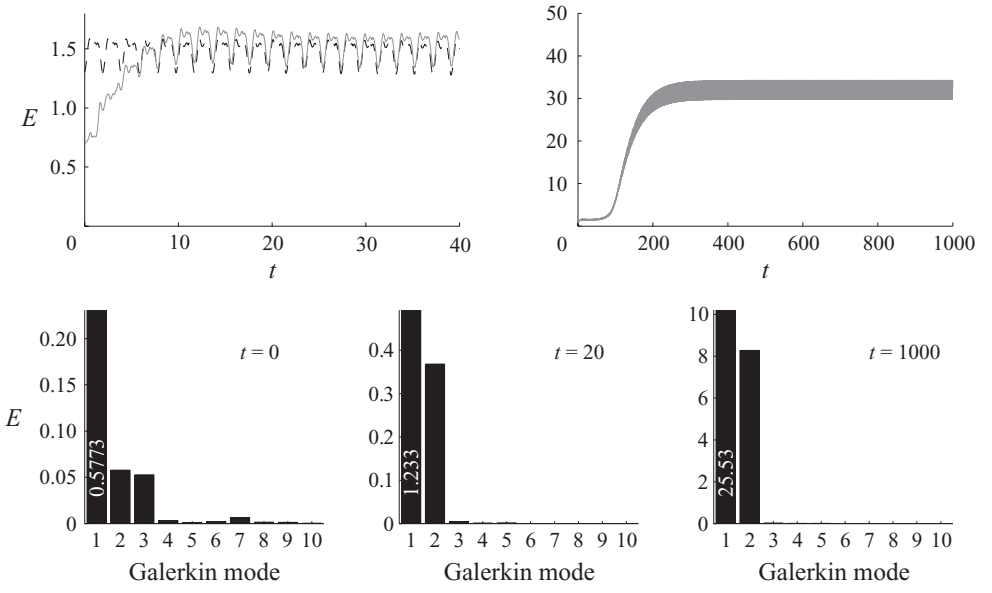

FIGURE 16. As for figure 15 but for system C.

100 time units ($E = 0.98$ for system B and $E = 1.28$ for system C) and then grow to the stable periodic solution at high energies ($E = 35.78$ for system B and $E = 29.74$ for system C). An inspection of the distribution of energy shows that the most dangerous initial states have significant energy in the higher order Galerkin modes, particularly the third mode, while the periodic solutions do not. Qualitatively, this evolution is identical to that seen for the first pair of periodic solutions at lower energy. Quantitatively, however, the transient energy growth is considerably larger. At $\beta = 0.75$, the most dangerous initial states have around 50 % of the minimum energy on the unstable periodic solution and around 1 % of the minimum energy on the stable periodic solution.

8. Conclusions

It is well known that some linearly stable thermoacoustic systems can trigger to self-sustained oscillations when perturbed with a sufficiently large impulse (Zinn & Lieuwen 2005). The most important characteristic of such systems is a subcritical bifurcation (Ananthkrishnan *et al.* 2005), which cannot be identified with a linear stability analysis. Triggering can occur in the region that is sometimes known as 'linearly stable but nonlinearly unstable', which is between β_s and β_H in figure 1. In this region, there are two (or more) stable solutions to the governing equations: a stable periodic solution and a stable fixed point (§ 3.1).

Triggering is usually caused by large-amplitude disturbances, such as a bomb placed within a combustion chamber. This is easy to explain: the large-amplitude impulse pushes the system from the basin of attraction of the stable fixed point to that of the stable periodic solution. Triggering can also be caused by small-amplitude disturbances, of the order of the background noise level (Zinn & Lieuwen 2005). In this paper, this is explained by drawing an analogy with bypass transition to turbulence in hydrodynamics.

Bypass transition in hydrodynamics explains the mechanism through which small perturbations can lead to turbulence in linearly stable flows. In many flows, the linear stability operator around the laminar solution is non-normal, which means that some initial states grow transiently even when the system is linearly stable. These states evolve towards periodic or quasi-periodic travelling-wave solutions, which are unstable and which then lead to turbulence (§ 1.1).

In this paper, it is shown that thermoacoustic systems evolve in a similar way. In brief, there is an unstable periodic solution between β_s and β_H, which plays a role similar to that of the unstable periodic travelling-wave solutions in hydrodynamics (§ 3.2). Initial states can be found that grow transiently around this unstable periodic solution before being repelled towards the stable periodic solution. These initial states have lower energy than both periodic solutions. In this paper, it is shown that these states initially exploit non-normal linear transient growth around the unstable periodic solution and then exploit the nonlinear dynamics to grow from there to the stable periodic solution. The latter process can be predicted with a nonlinear normal analysis (Noiray *et al.* 2008), but the former process cannot. In other words, non-normality describes the start of the journey, while nonlinearity describes the end.

In more detail, the monodromy matrix around the unstable periodic solution has one unstable eigenvalue, as required, but is also non-normal (§ 3.3). This means that, over one cycle, some perturbations around the unstable periodic solution grow faster than the perturbation in the direction of the unstable eigenvector. The perturbation that has maximum linear growth over one cycle is found from the SVD of the monodromy matrix (figure 6 and table 1). This information is useful but is limited because it comes from a linear analysis. In this paper, a procedure is developed (§ 4) that uses the nonlinear governing equations to find the lowest energy initial state that evolves to the stable periodic solution (figure 9 and table 3). This is called the 'most dangerous' initial state. It is broadly similar to a combination of the lowest energy point on the unstable periodic solution (figure 4 and table 1) and the optimal linear perturbation found from the monodromy matrix (figure 6 and table 2). In particular, it has high amplitudes in the first, third and fourth modes. It is different from the state with maximal transient growth around the stable fixed point (figure 7), which has been found in previous studies (Balasubramanian & Sujith 2008*a*), but which does not lead to triggering from the lowest possible initial energy (Juniper 2010). It is also found that nonlinearity contributes as much as non-normality to transient growth, which differs from hydrodynamics, in which the nonlinear terms conserve energy. Furthermore, in this model, the boundary between states that decay to the zero solution and states that grow to a stable periodic solution is much simpler than that found in fluid mechanical systems. The evidence for this is that states from a broad range of initial conditions grow transiently to one of two unstable periodic solutions, rather than several unstable periodic solutions, before growing to one of two stable periodic solutions or decaying to the stable fixed point.

The most dangerous initial states have been calculated between β_s and β_H in order to determine the perturbation energy below which all states decay to the stable fixed point (figure 13). This is called the 'safe operating region'. It is found to be much smaller than would be predicted by a linear analysis and slightly smaller than would be predicted by a nonlinear normal analysis. More realistic models of thermoacoustic systems have much higher non-normality than the model used in this paper; so it is likely that the safe operating region between β_s and β_H is smaller still.

This paper describes the mechanism through which perturbations with small amplitudes can reach stable periodic solutions with large amplitudes. The analysis,

however, assumes that a perfectly defined impulse can be imposed onto a perfectly quiet system, which is unrealistic. It is more realistic to examine the effect of continuous noise on a non-normal system. In Waugh & Juniper (2010), noise with spectral characteristics similar to the most dangerous initial state is imposed onto the model used in this paper. The noise amplitude is increased until the system triggers to the stable periodic solution. The triggering process follows exactly that which is expected from this paper: the system starts around the stable fixed point, then jumps to the unstable periodic solution and then grows to the stable periodic solution. This compares well with experimental results of low-amplitude triggering such as figure 15(*b*) of Lieuwen (2002).

From an engineering point of view, it is important to know whether non-normality and transient growth are likely to be influential in triggering self-sustained oscillations in real thermoacoustic systems. Real thermoacoustic systems have transient growth that is several orders of magnitude higher than that in a Rijke tube. With sufficient computing power, the techniques presented in this paper could be used to calculate the safe operating regions of more accurate models of thermoacoustic systems. Even without this step, however, one practical conclusion of this study is that, in systems that are linearly stable, one must look for nonlinear self-sustained oscillations because it may take surprisingly little initial energy for the system to find a way to reach them.

I would like to thank P. Schmid for patiently helping at numerous stages during this project, particularly with implementation of the nonlinear adjoint looping and conjugate gradient algorithms. I am very grateful to R. I. Sujith and S. Nagaraja for helpful and enthusiastic discussions from the start of this project and for providing the Matlab code that they used in Balasubramanian & Sujith (2008*a*). I would like to thank S. Mariappan and P. Subramanian for introducing me to DDE-Biftool and I. Waugh and M. Geuss for mastering it. I would also like to thank A. Bottaro for explaining the principles of nonlinear adjoint looping, and P. Huerre and P. Schmid for their very clear notes on Optimal Control. This work was supported by EPSRC and the Advanced Instability Methods (AIM) Network under grants EP/G033803/1 and EP/GO37779/1.

Appendix A. Constrained optimization

In this appendix, the equations for constrained optimization are derived for the continuous nonlinear governing equations with cost functional $\mathfrak{J}_{av} \equiv E_{av}/E_0$. Appendix B contains all other variations of these equations: for linear and nonlinear governing equations; in continuous and discrete form; and for cost functionals $\mathfrak{J}_{av}$ and $\mathfrak{J}_T$.

A.1. *Definitions*

The following inner products are defined:

$$\langle g, h \rangle \equiv \frac{1}{X} \int_0^X gh \, \mathrm{d}x, \tag{A 1}$$

$$\{g, h\} \equiv \frac{1}{T} \int_0^T gh \, \mathrm{d}t, \tag{A 2}$$

$$[g, h] \equiv \frac{1}{XT} \int_0^X \int_0^T gh \, \mathrm{d}t \, \mathrm{d}x. \tag{A 3}$$

The cost functional is defined as the mean acoustic energy during time T divided by the initial acoustic energy:

$$\mathfrak{J} \equiv \frac{E_{av}}{E_0} = \frac{[u,u]+[p,p]}{\langle u_0,u_0\rangle+\langle p_0,p_0\rangle}. \tag{A 4}$$

The variation of $\mathfrak{J}$ with respect to variation in u, for instance, is defined as

$$\left[\frac{\partial \mathfrak{J}}{\partial u},\delta u\right] \equiv \lim_{\epsilon\to 0}\frac{\mathfrak{J}(u+\epsilon\delta u)-\mathfrak{J}(u)}{\epsilon}. \tag{A 5}$$

A.2. *The direct governing equations in continuous form*

The delayed velocity $v(x,t)\equiv u(x,t-\tau)$ is introduced into the governing equations (2.5) and (2.6) in order to separate the time delay term from the nonlinear term. This is not strictly necessary but it makes the derivation easier to present. The governing equations for $u(x,t)$ and $p(x,t)$ and the initial conditions for $u(x,0)$ and $p(x,0)$ are written in terms of functions that equal zero:

$$F_1(x,t) \equiv \frac{\partial u}{\partial t}+\frac{\partial p}{\partial x}=0, \tag{A 6}$$

$$F_2(x,t) \equiv \frac{\partial p}{\partial t}+\frac{\partial u}{\partial x}+\zeta p-\beta\left(\left|\frac{1}{3}+v_f\right|^{1/2}-\left(\frac{1}{3}\right)^{1/2}\right)\delta_D(x-x_f)=0, \tag{A 7}$$

$$F_3(x,t) \equiv v-u(t-\tau)=0, \tag{A 8}$$

$$G_1(x) \equiv u(0)-u_0=0, \tag{A 9}$$

$$G_2(x) \equiv p(0)-p_0=0. \tag{A 10}$$

Equations (A 9) and (A 10) are not necessary for the derivation of the adjoint equations but are included so that it is easier to extract the change in the cost functional with respect to changes in the initial conditions.

A.3. *Definition and re-arrangement of the Lagrangian functional*

The cost functional $\mathfrak{J}$ is to be maximized subject to the constraints (A 6)–(A 10). To achieve this, a Lagrangian functional, $\mathfrak{L}$, is defined with Lagrange multipliers $a(x,t)$, $b(x,t)$, $c(x,t)$, $d(x)$ and $e(x)$:

$$\mathfrak{L} \equiv \mathfrak{J}-[a,F_1]-[b,F_2]-[c,F_3]-\langle d,G_1\rangle-\langle e,G_2\rangle. \tag{A 11}$$

At optimality, the variations of $\mathfrak{L}$ with respect to variations in all of the variables must be zero.

The variations of $\mathfrak{L}$ with respect to variations in a, b, c, d and e are automatically zero if the governing equations (A 6)–(A 8) are satisfied for $x=[0,X]$ and $t=[0,T]$ and if the initial conditions (A 9)–(A 10) are satisfied for $x=[0,X]$ at $t=0$.

The variations of $\mathfrak{L}$ with respect to variations in u, p, v, u_0 and p_0 are calculated by re-arranging the terms on the right-hand side of (A 11). The contributions of the nonlinear terms in (A 11) are considered first.

One nonlinear term arises from $\mathfrak{J}$. Following the definition (A 5), the variations in $\mathfrak{J}$ with respect to variations in u, p, u_0 and p_0 are

$$\begin{aligned}\left[\frac{\partial \mathfrak{J}}{\partial u},\delta u\right] &= \frac{1}{\epsilon}\left(\frac{1}{XT}\int_0^T\int_0^X \frac{(u+\epsilon\delta u)^2}{2E_0}\,\mathrm{d}x\,\mathrm{d}t-\frac{1}{XT}\int_0^T\int_0^X\frac{u^2}{2E_0}\,\mathrm{d}x\,\mathrm{d}t\right)\\ &= \frac{1}{XT}\int_0^T\int_0^X\frac{2u}{2E_0}\,\delta u\,\mathrm{d}x\,\mathrm{d}t=\left[\frac{u}{E_0},\delta u\right],\end{aligned} \tag{A 12}$$

$$\left[\frac{\partial \mathfrak{J}}{\partial p}, \delta p\right] = \left[\frac{p}{E_0}, \delta p\right], \tag{A 13}$$

$$\left[\frac{\partial \mathfrak{J}}{\partial u_0}, \delta u_0\right] = \left[-\frac{u_0 E_{av}}{E_0^2}, \delta u_0\right], \tag{A 14}$$

$$\left[\frac{\partial \mathfrak{J}}{\partial p_0}, \delta p_0\right] = \left[-\frac{p_0 E_{av}}{E_0^2}, \delta p_0\right], \tag{A 15}$$

where $2E_0 \equiv \langle u_0, u_0\rangle + \langle p_0, p_0\rangle$ and $2E_{av} \equiv [u_0, u_0] + [p_0, p_0]$.

Another nonlinear term arises from $[b, F_2]$. The contribution to $\mathfrak{L}$ of this term, which is briefly labelled $\mathfrak{K}$, is

$$\mathfrak{K} \equiv -\left[b, -\beta\delta_D(x - x_f)\left(\left|\tfrac{1}{3} + v_f\right|^{1/2} - \left(\tfrac{1}{3}\right)^{1/2}\right)\right]. \tag{A 16}$$

The variation of $\mathfrak{K}$ with respect to variations in $v(x, t)$ is to be calculated, using the fact that

$$\left(\tfrac{1}{3} + (v_f + \epsilon\delta v_f)\right)^{1/2} = \left(\tfrac{1}{3} + v_f\right)^{1/2} + \tfrac{1}{2}\left(\tfrac{1}{3} + v_f\right)^{-1/2}\epsilon\delta v_f, \tag{A 17}$$

for infinitesimal ϵ, where δv_f is the variation of v evaluated at the hot wire position:

$$\delta v_f \equiv \int_0^X \delta v\ \delta_D(x - x_f)\,\mathrm{d}x. \tag{A 18}$$

As a reminder, δ represents a small variation and δ_D represents the Dirac delta. For $v_f \geqslant -1/3$, the variation of $\mathfrak{K}$ is

$$\begin{aligned}
\left[\frac{\partial \mathfrak{K}}{\partial v}, \delta v\right] &\equiv \lim_{\epsilon\to 0}\frac{\mathfrak{K}(v + \epsilon\delta v) - \mathfrak{K}(v)}{\epsilon} \\
&= -\left[b, -\beta\delta_D(x - x_f)\frac{1}{2}\left(\frac{1}{3} + v_f\right)^{-1/2}\delta v_f\right] \\
&= \frac{1}{XT}\int_0^X\int_0^T \beta b\delta_D(x - x_f)\frac{1}{2}\left(\frac{1}{3} + v_f\right)^{-1/2}\delta v_f\,\mathrm{d}t\,\mathrm{d}x \\
&= \frac{1}{XT}\int_0^T \beta b_f\frac{1}{2}\left(\frac{1}{3} + v_f\right)^{-1/2}\delta v_f\,\mathrm{d}t \\
&= \frac{1}{XT}\int_0^T \beta b_f\frac{1}{2}\left(\frac{1}{3} + v_f\right)^{-1/2}\int_0^X \delta v\ \delta_D(x - x_f)\,\mathrm{d}x\,\mathrm{d}t \\
&= \frac{1}{XT}\int_0^T\int_0^X \beta b_f\frac{1}{2}\left(\frac{1}{3} + v_f\right)^{-1/2}\delta v\ \delta_D(x - x_f)\,\mathrm{d}x\,\mathrm{d}t \\
&= \left[\beta b_f\frac{1}{2}\left(\frac{1}{3} + v_f\right)^{-1/2}\delta_D(x - x_f), \delta v\right].
\end{aligned} \tag{A 19}$$

For $v_f < -1/3$, the gradient changes sign due to the modulus in (A 16). To handle this, a sign function, σ, is placed in front of β in (A 19) such that $\sigma = +1$ for $v_f \geqslant -1/3$ and $\sigma = -1$ for $v_f < -1.3$. There are no more nonlinear terms.

The contributions of the linear terms in (A 11) are considered next. The inner products in terms of a, b, c, d and e are expanded, integrated by parts, re-arranged

and expressed as inner products in terms of u, p, v, u_0 and p_0:

$$\begin{aligned}
-[a,F_1] &= -\frac{1}{XT}\int_0^X\int_0^T a\frac{\partial u}{\partial t}\,\mathrm{d}t\,\mathrm{d}x - \frac{1}{XT}\int_0^X\int_0^T a\frac{\partial p}{\partial x}\,\mathrm{d}t\,\mathrm{d}x \\
&= -\frac{1}{XT}\int_0^X (a(T)u(T)-a(0)u(0))\,\mathrm{d}x + \frac{1}{XT}\int_0^X\int_0^T u\frac{\partial a}{\partial t}\,\mathrm{d}t\,\mathrm{d}x\cdots \\
&\quad -\frac{1}{XT}\int_0^T (p(X)a(X)-p(0)a(0))\,\mathrm{d}t + \frac{1}{XT}\int_0^X\int_0^T p\frac{\partial a}{\partial x}\,\mathrm{d}t\,\mathrm{d}x \\
&= -\left\langle\frac{a(T)}{T},u(T)\right\rangle + \left\langle\frac{a(0)}{T},u(0)\right\rangle + \left[\frac{\partial a}{\partial t},u\right]\cdots \\
&\quad -\left\{\frac{a(X)}{X},p(X)\right\} + \left\{\frac{a(0)}{X},p(0)\right\} + \left[\frac{\partial a}{\partial x},p\right]. \qquad \text{(A 20)}
\end{aligned}$$

$$\begin{aligned}
-[b,F_2] &= -\left\langle\frac{b(T)}{T},p(T)\right\rangle + \left\langle\frac{b(0)}{T},p(0)\right\rangle + \left[\frac{\partial b}{\partial t},p\right]\cdots \\
&\quad -\left\{\frac{b(X)}{X},u(X)\right\} + \left\{\frac{b(0)}{X},u(0)\right\} + \left[\frac{\partial b}{\partial x},u\right] - [\zeta b,p], \qquad \text{(A 21)}
\end{aligned}$$

$$-[c,F_3] = -[c,v] + [c,u(t-\tau)], \qquad \text{(A 22)}$$

$$-\langle d,G_1\rangle = -\langle d,u(0)\rangle + \langle d,u_0\rangle, \qquad \text{(A 23)}$$

$$-\langle e,G_2\rangle = -\langle e,p(0)\rangle + \langle e,p_0\rangle. \qquad \text{(A 24)}$$

The last term in (A 22) needs to be expressed in terms of $u(t)$, rather than $u(t-\tau)$, before it can be combined with the other terms. This is achieved with a change of variable $t' \equiv t-\tau$ and a change in the limits of the time integration:

$$\begin{aligned}
[c,u(t-\tau)] &= \frac{1}{XT}\int_0^T\int_0^X c(t)u(t-\tau)\,\mathrm{d}x\,\mathrm{d}t \\
&= \frac{1}{XT}\int_{-\tau}^{T-\tau}\int_0^X c(t'+\tau)u(t')\,\mathrm{d}x\,\mathrm{d}t' \\
&= \frac{1}{XT}\int_{-\tau}^{0}\int_0^X c(t'+\tau)u(t')\,\mathrm{d}x\,\mathrm{d}t' + \frac{1}{XT}\int_0^{T-\tau}\int_0^X c(t'+\tau)u(t')\,\mathrm{d}x\,\mathrm{d}t' \\
&= [c(t+\tau),u]_{-\tau}^{0} + [c(t+\tau),u]_{0}^{T-\tau} + [0,u]_{T-\tau}^{T}. \qquad \text{(A 25)}
\end{aligned}$$

The boundary conditions for pressure require that $p(X)=p(0)=0$ and the boundary conditions for adjoint pressure require that $b(X)=b(0)=0$; so the terms in curly braces in (A 20) and (A 21) are zero.

For the linear terms, the variations can be written down by inspection. (For example, in (A 20) u is simply replaced with δu.) Gathering together all the contributions from (A 12)–(A 15) and (A 19)–(A 25) gives

$$\begin{aligned}
\left[\frac{\partial\mathfrak{L}}{\partial u},\delta u\right] &= \left[\left(\frac{u}{E_0}+\frac{\partial a}{\partial t}+\frac{\partial b}{\partial x}+c(t+\tau)\right),\delta u\right]_0^{T-\tau} + \left[\left(\frac{u}{E_0}+\frac{\partial a}{\partial t}+\frac{\partial b}{\partial x}\right),\delta u\right]_{T-\tau}^{T}\cdots \\
&\quad + [c(t+\tau),\delta u]_{-\tau}^{0} - \left\langle\frac{a(T)}{T},\delta u(T)\right\rangle + \left\langle\left(\frac{a(0)}{T}-d\right),\delta u(0)\right\rangle, \qquad \text{(A 26)}
\end{aligned}$$

$$\left[\frac{\partial\mathfrak{L}}{\partial p},\delta p\right] = \left[\left(\frac{p}{E_0}+\frac{\partial b}{\partial t}+\frac{\partial a}{\partial x}-\zeta b,\delta p\right)\right]_0^T - \left\langle\frac{b(T)}{T},\delta p(T)\right\rangle + \left\langle\frac{b(0)}{T}-e,\delta p(0)\right\rangle, \qquad \text{(A 27)}$$

$$\left[\frac{\partial \mathfrak{L}}{\partial v}, \delta v\right] = \left[\sigma\beta b_f \frac{1}{2}\left(\frac{1}{3}+v_f\right)^{-1/2}\delta_D(x-x_f) - c, \delta v\right]_0^T, \tag{A 28}$$

$$\left\langle \frac{\partial \mathfrak{L}}{\partial u_0}, \delta u_0 \right\rangle = \left\langle d - \frac{u_0 E_{av}}{E_0^2}, \delta u_0 \right\rangle, \tag{A 29}$$

$$\left\langle \frac{\partial \mathfrak{L}}{\partial p_0}, \delta p_0 \right\rangle = \left\langle e - \frac{p_0 E_{av}}{E_0^2}, \delta p_0 \right\rangle. \tag{A 30}$$

A.4. *The adjoint governing equations in continuous form*

At optimality, (A 26)–(A 30) must equal zero for any δu, δp and δv. This leads to the optimality conditions, which will be presented in the next section, and the adjoint governing equations, which must be satisfied for $x = [0, x]$ and $t = [0, T]$:

$$b_f = 0, \quad \text{for } t = [0, \tau], \tag{A 31}$$

$$F_1^+ \equiv \frac{\partial a}{\partial t} + \frac{\partial b}{\partial x} + \frac{u}{E_0} + \sigma\beta b_f(t+\tau)\frac{1}{2}\cdots \times \left(\frac{1}{3}+u_f(t)\right)^{-1/2}\delta_D(x-x_f) = 0, \quad \text{for } t = [0, T-\tau], \tag{A 32}$$

$$F_1^+ \equiv \frac{\partial a}{\partial t} + \frac{\partial b}{\partial x} + \frac{u}{E_0} = 0, \quad \text{for } t = (T-\tau, T], \tag{A 33}$$

$$F_2^+ \equiv \frac{\partial b}{\partial t} + \frac{\partial a}{\partial x} + \frac{p}{E_0} - \zeta b = 0, \quad \text{for } t = [0, T]. \tag{A 34}$$

A.5. *The optimality conditions at $t = 0$ and $t = T$*

Similarly, the requirement that (A 26)–(A 30) must equal zero for any δu, δp and δv leads to the optimality condition at $t = T$:

$$a(T) = 0, \qquad b(T) = 0, \tag{A 35}$$

which can be thought of as the initialization of the adjoint variables It also leads to an optimality condition at $t = 0$, which is later used to find gradient information:

$$d = \frac{a(0)}{T}, \qquad e = \frac{b(0)}{T}. \tag{A 36}$$

A.6. *Gradient information*

The gradient information $\partial\mathfrak{L}/\partial u_0$ and $\partial\mathfrak{L}/\partial p_0$ is found by combining (A 29) and (A 30) with (A 36):

$$\frac{\partial \mathfrak{L}}{\partial u_0} = \frac{a(0)}{T} - \frac{E_{av}}{E_0^2}u_0, \tag{A 37}$$

$$\frac{\partial \mathfrak{L}}{\partial p_0} = \frac{b(0)}{T} - \frac{E_{av}}{E_0^2}p_0. \tag{A 38}$$

If (A 31)–(A 35) are satisfied, then $\partial\mathfrak{J}/\partial u_0 = \partial\mathfrak{L}/\partial u_0$ and $\partial\mathfrak{J}/\partial p_0 = \partial\mathfrak{L}/\partial p_0$, subject to the constraints, which means that (A 37) and (A 38) give gradient information about $\mathfrak{J}$ with respect to the initial conditions u_0 and p_0. This information is used in a convenient optimization routine in order to find the point where $\partial\mathfrak{J}/\partial u_0 = 0$ and $\partial\mathfrak{J}/\partial p_0 = 0$, subject to the constraints, which is the optimal point.

Appendix B. Catalogue of all the equations required for optimization

This appendix contains the direct governing equations, adjoint governing equations, optimality conditions and gradient information for the Rijke tube in the following cases: linear and nonlinear; continuous and discrete; cost functionals $\mathfrak{J}_{av}$ and $\mathfrak{J}_T$.

B.1. *Definitions*

Inner products:

$$\langle g,h\rangle \equiv \frac{1}{X}\int_0^X gh\,\mathrm{d}x, \quad \{g,h\} \equiv \frac{1}{T}\int_0^T gh\,\mathrm{d}t, \quad [g,h] \equiv \frac{1}{XT}\int_0^X\int_0^T gh\,\mathrm{d}t\,\mathrm{d}x. \tag{B 1}$$

Cost functionals:

$$\mathfrak{J}_{av} \equiv \frac{E_{av}}{E_0} = \frac{[u,u]+[p,p]}{\langle u_0,u_0\rangle+\langle p_0,p_0\rangle}, \qquad \mathfrak{J}_T \equiv \frac{E_T}{E_0} = \frac{\langle u,u\rangle+\langle p,p\rangle}{\langle u_0,u_0\rangle+\langle p_0,p_0\rangle}. \tag{B 2}$$

Basis sets for discretization:

$$u = \sum_{j=1}^{N} \eta_j \cos(j\pi x), \qquad p = -\sum_{j=1}^{N}\left(\frac{\dot{\eta}_j}{j\pi}\right)\sin(j\pi x). \tag{B 3}$$

The variables a and b, respectively, represent the adjoint velocity and pressure and have the same boundary conditions as u and p, respectively. They are discretized in a way similar to u and p:

$$a = \sum_{j=1}^{N}\left(\frac{\xi_j}{j\pi}\right)\cos(j\pi x), \qquad b = -\sum_{j=1}^{N}\nu_j \sin(j\pi x). \tag{B 4}$$

The following abbreviations are defined: $s_j \equiv \sin(j\pi x_f)$ and $c_j \equiv \cos(j\pi x_f)$.

B.2. *Direct governing equations in continuous form*

Nonlinear:

$$F_1 \equiv \frac{\partial u}{\partial t} + \frac{\partial p}{\partial x} = 0, \tag{B 5}$$

$$F_2 \equiv \frac{\partial p}{\partial t} + \frac{\partial u}{\partial x} + \zeta p - \beta\left(\left|\frac{1}{3}+u_f(t-\tau)\right|^{1/2} - \left(\frac{1}{3}\right)^{1/2}\right)\delta_D(x-x_f) = 0. \tag{B 6}$$

Linear:

$$F_1 \equiv \frac{\partial u}{\partial t} + \frac{\partial p}{\partial x} = 0, \tag{B 7}$$

$$F_2 \equiv \frac{\partial p}{\partial t} + \frac{\partial u}{\partial x} + \zeta p - \beta\frac{\sqrt{3}}{2}\left(u_f - \tau\frac{\partial u_f}{\partial t}\right)\delta_D(x-x_f) = 0. \tag{B 8}$$

B.3. *Direct governing equations in discrete form*

Nonlinear:

$$F_{1G} \equiv \frac{\mathrm{d}}{\mathrm{d}t}\eta_j - j\pi\left(\frac{\dot{\eta}_j}{j\pi}\right) = 0, \tag{B 9}$$

$$F_{2G} \equiv \frac{\mathrm{d}}{\mathrm{d}t}\left(\frac{\dot{\eta}_j}{j\pi}\right) + j\pi\eta_j + \zeta_j\left(\frac{\dot{\eta}_j}{j\pi}\right) + 2\beta\left(\left|\frac{1}{3} + u_f(t-\tau)\right|^{1/2} - \left(\frac{1}{3}\right)^{1/2}\right)s_j = 0, \tag{B 10}$$

where $u_f(t-\tau) = \sum_{k=1}^{N} \eta_k(t-\tau)c_k$.

Linear:

$$F_{1G} \equiv \frac{\mathrm{d}}{\mathrm{d}t}\eta_j - j\pi\left(\frac{\dot{\eta}_j}{j\pi}\right) = 0, \tag{B 11}$$

$$F_{2G} \equiv \frac{\mathrm{d}}{\mathrm{d}t}\left(\frac{\dot{\eta}_j}{j\pi}\right) + j\pi\eta_j + \zeta_j\left(\frac{\dot{\eta}_j}{j\pi}\right) + \sqrt{3}\beta s_j \sum_{k=1}^{N}\eta_k(t)c_k - \sqrt{3}\beta\tau s_j \sum_{k=1}^{N} k\pi\left(\frac{\dot{\eta}_k}{k\pi}\right)c_k = 0. \tag{B 12}$$

B.4. *Adjoint governing equations in continuous form*

Nonlinear, with cost functional $\mathfrak{J}_{av}$:

$$b_f = 0, \quad \text{for } t = [0, \tau], \tag{B 13}$$

$$F_1^+ \equiv \frac{\partial a}{\partial t} + \frac{\partial b}{\partial x} + \frac{u}{E_0} + \sigma\beta b_f(t+\tau)\frac{1}{2}\cdots \times\left(\frac{1}{3} + u_f(t)\right)^{-1/2}\delta_D(x - x_f) = 0, \quad \text{for } t = [0, T-\tau], \tag{B 14}$$

$$F_1^+ \equiv \frac{\partial a}{\partial t} + \frac{\partial b}{\partial x} + \frac{u}{E_0} = 0, \quad \text{for } t = (T-\tau, T], \tag{B 15}$$

$$F_2^+ \equiv \frac{\partial b}{\partial t} + \frac{\partial a}{\partial x} + \frac{p}{E_0} - \zeta b = 0, \quad \text{for } t = [0, T]. \tag{B 16}$$

Linear, with cost functional $\mathfrak{J}_{av}$:

$$F_1^+ \equiv \frac{\partial a}{\partial t} + \frac{\partial b}{\partial x} + \frac{u}{E_0} + \frac{\sqrt{3}}{2}\beta\left(b_f + \tau\frac{\partial b_f}{\partial t}\right)\delta_D(x - x_f) = 0, \quad \text{for } t = [0, T], \tag{B 17}$$

$$F_2^+ \equiv \frac{\partial b}{\partial t} + \frac{\partial a}{\partial x} + \frac{p}{E_0} - \zeta b = 0, \quad \text{for } t = [0, T]. \tag{B 18}$$

When the cost functional is $\mathfrak{J}_T$, the u/E_0 and p/E_0 terms are dropped.

B.5. *Derivation of the adjoint governing equations in discrete form*

The discretized adjoint governing equations can be derived in two ways. The first way is to derive the continuous adjoint equations, as in § B.4, and then discretize them with (B 4). This is known as 'optimize then discretize' (OTD) in Bewley (2001) and 'finite difference of adjoint' in Sirkes & Tziperman (1997). The second way is to discretize the direct governing equations, as in § B.3, and then derive the adjoint of the discretized equations. This is known as 'discretize then optimize' (DTO) in Bewley (2001) and 'adjoint of finite difference' in Sirkes & Tziperman (1997). To achieve this, Lagrange multipliers $\xi_j/(j\pi)$ should be used for the series of F_{1G} equations and ν_j for the series of F_{2G} equations.

OTD has the advantage that the continuous adjoint equations are relatively easy to derive and that, once they have been derived, any discretization scheme can

be applied to them. This advantage is not useful in this paper because only one discretization scheme is considered. However, it has the disadvantage that the adjoint discretization can differ from the direct discretization, which leads to inaccurate gradient information.

DTO has the advantage that the direct discretized equations and the adjoint discretized equations share the same discretization scheme and therefore share the same truncation errors. In other words, this route provides perfect gradient information for a set of imperfect equations. In the linear case, this adjoint is given by ($\boldsymbol{L}^+ = -\boldsymbol{L}^H$), which makes the linear code easy to implement.

The two routes described above, OTD and DTO, do not necessarily give the same discretized adjoint governing equations, although the solutions of these equations should approach each other as the resolution of the discretization increases. For the governing equations in this paper, both routes give the same discretized adjoint governing equations for the nonlinear case but different discretized adjoint governing equations for the linear case. For the linear case, DTO is chosen.

B.6. *Adjoint governing equations in discrete form*

Nonlinear, with cost functional $\mathfrak{J}_{av}$, through both OTD and DTO:

$$b_f = 0, \quad \text{for } t = [0, \tau], \tag{B 19}$$

$$F^+_{1G} \equiv \frac{\mathrm{d}}{\mathrm{d}t}\left(\frac{\xi_j}{j\pi}\right) - j\pi\nu_j + \frac{\eta_j}{E_0} + \sigma\beta b_f(t+\tau)\left|\frac{1}{3} + u_f(t)\right|^{-1/2} c_j = 0, \quad \text{for } t = [0, T-\tau], \tag{B 20}$$

$$F^+_{1G} \equiv \frac{\mathrm{d}}{\mathrm{d}t}\left(\frac{\xi_j}{j\pi}\right) - j\pi\nu_j + \frac{\eta_j}{E_0}, \quad \text{for } t = (T-\tau, T], \tag{B 21}$$

$$F^+_{2G} \equiv \frac{\mathrm{d}}{\mathrm{d}t}\nu_j + j\pi\left(\frac{\xi_j}{j\pi}\right) - \frac{1}{E_0}\left(\frac{\dot{\eta}_j}{j\pi}\right) - \zeta_j\nu_j = 0, \quad \text{for } t = [0, T], \tag{B 22}$$

where

$$u_f(t) = \sum_{j=1}^{\infty} \eta_j(t)c_j, \qquad b_f(t+\tau) = -\sum_{j=1}^{\infty} \nu_j(t+\tau)s_j. \tag{B 23}$$

Linear, with cost functional $\mathfrak{J}_{av}$, through DTO:

$$F^+_{1G} \equiv \frac{\mathrm{d}}{\mathrm{d}t}\left(\frac{\xi_j}{j\pi}\right) - j\pi\nu_j + \frac{\eta_j}{E_0} + \sqrt{3}\beta c_j \sum_{k=1}^{N} \nu_k s_k = 0, \tag{B 24}$$

$$F^+_{2G} \equiv \frac{\mathrm{d}}{\mathrm{d}t}\nu_j + j\pi\left(\frac{\xi_j}{j\pi}\right) - \frac{1}{E_0}\left(\frac{\dot{\eta}_j}{j\pi}\right) - \zeta_j\nu_j - \sqrt{3}j\pi\beta\tau c_j \sum_{k=1}^{N} \nu_k s_k = 0. \tag{B 25}$$

When the cost functional is $\mathfrak{J}_T$, the η_j/E_0 and $(\dot{\eta}_j/j\pi)/E_0$ terms are dropped.

B.7. *Optimality conditions*

Optimality conditions at $t = T$ for the cost functional $\mathfrak{J}_{av}$ in continuous form,

$$a(T) = 0, \qquad b(T) = 0, \tag{B 26}$$

and in discrete form,

$$\xi_j(T) = 0, \qquad \nu_j(T) = 0. \tag{B 27}$$

Optimality conditions at $t = T$ for the cost functional $\mathfrak{J}_T$ in continuous form,

$$a(T) = \frac{2T}{E_0} u(T), \qquad b(T) = \frac{2T}{E_0} p(T), \tag{B 28}$$

and in discrete form,

$$\xi_j(T)/(j\pi) = \frac{2T}{E_0} \eta_j(T), \qquad \nu_j(T) = \frac{2T}{E_0} \dot{\eta}_j(T)/(j\pi). \tag{B 29}$$

These apply to both the linear and the nonlinear governing equations.

B.8. *Gradient information*

Gradient information at $t = 0$ for the cost functional $\mathfrak{J}_{av}$ in continuous form,

$$\frac{\partial \mathfrak{L}}{\partial u_0} = \frac{a(0)}{T} - \frac{E_{av}}{E_0^2} u_0, \qquad \frac{\partial \mathfrak{L}}{\partial p_0} = \frac{b(0)}{T} - \frac{E_{av}}{E_0^2} p_0, \tag{B 30}$$

and in discrete form,

$$\frac{\partial \mathfrak{L}}{\partial \eta_{0_j}} = \frac{1}{T}\left(\frac{\xi_j(0)}{j\pi}\right) - \frac{E_{av}}{E_0^2}\eta_{0_j}, \qquad \frac{\partial \mathfrak{L}}{\partial(\dot{\eta}_{0_j}/j\pi)} = \frac{\nu_j(0)}{T} - \frac{E_{av}}{E_0^2}\left(\frac{\dot{\eta}_{0_j}}{j\pi}\right). \tag{B 31}$$

Gradient information at $t = 0$ for the cost functional $\mathfrak{J}_T$ in continuous form,

$$\frac{\partial \mathfrak{L}}{\partial u_0} = \frac{a(0)}{T} - 2\frac{E_T}{E_0^2} u_0, \qquad \frac{\partial \mathfrak{L}}{\partial p_0} = \frac{b(0)}{T} - 2\frac{E_T}{E_0^2} p_0, \tag{B 32}$$

and in discrete form,

$$\frac{\partial \mathfrak{L}}{\partial \eta_{0_j}} = \frac{1}{T}\left(\frac{\xi_j(0)}{j\pi}\right) - 2\frac{E_T}{E_0^2}\eta_{0_j}, \qquad \frac{\partial \mathfrak{L}}{\partial(\dot{\eta}_{0_j}/j\pi)} = \frac{\nu_j(0)}{T} - 2\frac{E_T}{E_0^2}\left(\frac{\dot{\eta}_{0_j}}{j\pi}\right). \tag{B 33}$$

These apply to both the linear and the nonlinear governing equations.

REFERENCES

Ananthkrishnan, N., Deo, S. & Culick, F. 2005 Reduced-order modeling and dynamics of nonlinear acoustic waves in a combustion chamber. *Combust. Sci. Technol.* **177**, 221–247.

Ashwin, P. & Timme, M. 2005 Unstable attractors: existence and robustness in networks of oscillators with delayed pulse coupling. *Nonlinearity* **18** (5), 2035–2060.

Balasubramanian, K. & Sujith, R. I. 2008*a* Thermoacoustic instability in a Rijke tube: non-normality and nonlinearity. *Phys. Fluids* **20**, 044103.

Balasubramanian, K. & Sujith, R. I. 2008*b* Non-normality and nonlinearity in combustion–acoustic interaction in diffusion flames. *J. Fluid Mech.* **594**, 29–57.

Bewley, T. 2001 Flow control: new challenges for a new Renaissance. *Prog. Aerosp. Sci.* **37**, 21–58.

Butler, K. M. & Farrell, B. F. 1992 Three-dimensional optimal perturbations in viscous shear flow. *Phys. Fluids* A **4** (8), 1637–1650.

Dowling, A. P. 1997 Nonlinear self-excited oscillations of a ducted flame. *J. Fluid Mech.* **346**, 271–290.

Dowling, A. P. 1999 A kinematic model of a ducted flame. *J. Fluid Mech.* **394**, 51–72.

Duguet, Y., Willis, A. P. & Kerswell, R. R. 2008 Transition in pipe flow: the saddle structure on the boundary of turbulence. *J. Fluid Mech.* **613**, 255–274.

Engelborghs, K., Luzyanina, T. & Roose, D. 2002 Numerical bifurcation analysis of delay differential equations using DDE-BIFTOOL. *ACM Trans. Math. Softw.* **28** (1), 1–21.

Heckl, M. 1990 Nonlinear acoustic effects in the Rijke tube. *Acustica* **72**, 63.

Henningson, D. S. & Reddy, S. C. 1994 On the role of linear mechanisms in transition to turbulence. *Phys. Fluids* **6** (3), 1396–1398.

Jahnke, C. C. & Culick, F. E. C. 1994 Application of dynamical systems theory to nonlinear combustion instabilities. *J. Propul. Power* **10**, 508–517.

Juniper, M. P. 2010 Transient growth in the horizontal Rijke tube: nonlinear optimal initial states. In *N3L International Workshop T.U.M. Munich, Germany*.

Juniper, M. P. & Waugh, I. C. 2010 Bypass transition to sustained thermoacoustic oscillations in a linearly stable Rijke tube. In *16th AIAA/CEAS Aeroacoustics Conference, KTH, Stockholm, Sweden*. AIAA.

Landau, L. D. & Lifshitz, E. M. 1959 *Fluid Mechanics*. Pergamon.

Lieuwen, T. 2002 Experimental investigation of limit-cycle oscillations in an unstable gas turbine combustor. *J. Propul. Power* **18** (1), 61–67.

Matveev, I. 2003 Thermo-acoustic instabilities in the Rijke tube: experiments and modeling. PhD thesis, CalTech, Pasadena, CA.

Nagaraja, S., Kedia, K. & Sujith, R. I. 2009 Characterizing energy growth during combustion instabilities: singular values or eigenvalues? *Proc. Combust. Inst.* **32**, 2933–2940.

Nicoud, F., Benoit, L., Sensiau, C. & Poinsot, T. 2007 Acoustic modes in combustors with complex impedances and multidimensional active flames. *AIAA J.* **45** (2), 426–441.

Noiray, N., Durox, D., Schuller, T. & Candel, S. M. 2008 A unified framework for nonlinear combustion instability analysis based on the flame describing function. *J. Fluid Mech.* **615**, 139–167.

Press, H. P., Teukolsky, S. A., Vetterling, W. T. & Flannery, B. P. 1992 *Numerical Recipes in Fortran 77*. Cambridge University Press.

Reddy, S. C. & Henningson, D. S. 1993 Energy growth in viscous channel flows. *J. Fluid Mech.* **252**, 209–238.

Schmid, P. J. 2007 Nonmodal stability theory. *Annu. Rev. Fluid Mech.* **39**, 129–162.

Schmid, P. J. & Henningson, D. S. 2001 *Stability and Transition in Shear Flows*. Springer.

Schneider, T. M., Eckhardt, B. & Yorke, J. A. 2007 Turbulence transition and the edge of chaos in pipe flow. *Phys. Rev. Lett.* **99**, 034502.

Selimefendigila, F., Sujith, R. I. & Polifke, W. 2010 Identification of heat transfer dynamics for non-modal analysis of thermoacoustic stability. *Appl. Maths Comput.* (in press). doi:10.1016/j.amc.2010.07.051.

Sirkes, Z. & Tziperman, E. 1997 Finite difference of adjoint or adjoint of finite difference? *Mon. Weather Rev.* **125**, 3373–3378.

Skufca, J. D., Yorke, J. A. & Eckhardt, B. 2006 Edge of chaos in a parallel shear flow. *Phys. Rev. Lett.* **96**, 174101.

Strogatz, S. H. 2001 *Nonlinear Dynamics and Chaos*. Westview Press.

Subramanian, P., Mariappan, S., Sujith, R. I. & Wahi, P. 2010 Application of numerical continuation to bifurcation analysis of Rijke tube. In *N3L International Workshop T.U.M. Munich, Germany*.

Trefethen, L. N., Trefethen, A. E., Reddy, S. C. & Driscoll, T. A. 1993 Hydrodynamic stability without eigenvalues. *Science* **261**, 578–584.

Waugh, I. C. & Juniper, M. P. 2010 Triggering, bypass transition and the effect of noise on a linearly stable thermoacoustic system. *Proc. Combust. Inst.* **33** (in press). doi:10.1016/j.proci.2010.06.018.

Zinn, B. T. & Lieuwen, T. C. 2005 Combustion instability: basic concepts. In *Combustion Instabilities in Gas Turbine Engines* (ed. T. C. Lieuwen & V. Yang). AIAA.